

CHAPTER 4

RESULTS AND DISCUSSIONS

4.1 Characterization of zinc waste

4.1.1. Chemical compositions

Initially the chemical composition of zinc waste was analyzed quantitatively by XRF. The compositions in weight percent of oxides are shown in Table 4.1.

Table 4.1 Chemical compositions of zinc waste analyzed by XRF

Oxides	SiO ₂	Al ₂ O ₃	Fe ₂ O ₃	CaO	MgO	K ₂ O	ZnO	CuO
%wt	22.45	3.96	7.32	16.43	0.29	0.63	3.09	0.07
Oxides	PbO	TiO ₂	MnO	P ₂ O ₅	ZrO ₂	SO ₃	L.O.I	
%wt	1.07	0.10	0.10	0.21	0.01	30.64	13.94	

Zinc waste was composed of three main oxides, which were SiO₂, CaO and SO₃, with respect to the zinc refinery process as described in Chapter 2. SiO₂, CaO and SO₃ came from silicate, limestone and sulfuric acid (H₂SO₄) used in the process, respectively. The chemical compositions of zinc waste were also qualitatively analyzed by the EDS spectra, in terms of elements, as shown in Fig. 4.1.

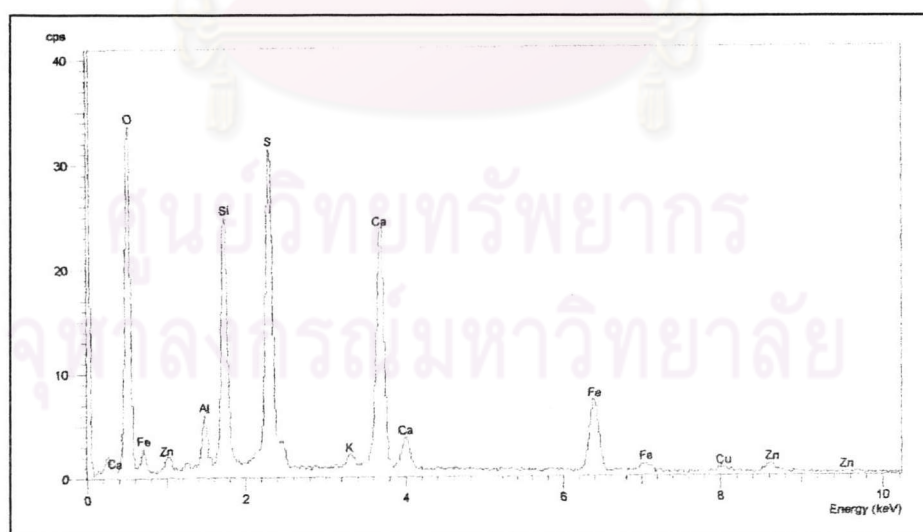


Fig.4.1 EDS spectra of zinc waste

Comparing to European zinc waste, zinc waste from Tak plant contained only ~7% of iron oxide but large amounts of CaO, SiO₂ and SO₃. Therefore, zinc waste from the Tak plant is not considered as an iron rich waste. It is believed that the differences in the zinc refinery process caused the difference in zinc waste compositions.

Since the high percentage of SO₃ in zinc waste was decomposed into sulfur dioxide (SO₂) which is toxic and hazardous at elevated temperature during glass melting, it is necessary to remove SO₂ from zinc waste prior to making glass. In order to remove SO₂, the thermal properties of zinc waste were analyzed to determine the suitable calcining temperature.

4.1.2. Thermal properties

Thermal properties of zinc waste were investigated by TG/DTA technique as shown in Fig.4.2 from room temperature to 1400°C. The percent weight loss of zinc waste, which is shown in the blue line, is associated with the change in endothermic and exothermic energy, which are shown in the red line.

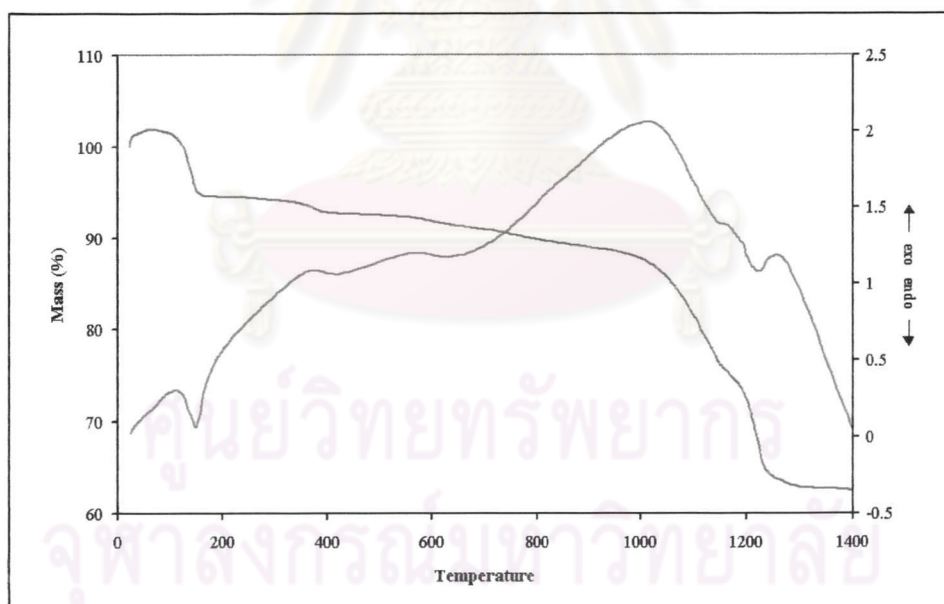


Fig. 4.2 Thermal properties of zinc waste analyzed by TG/DTA

To consider the change in percent weight loss and energies in certain temperature regions, the TG/DTA data was split into four different temperature regions at 100°C-190°C, 300°C-415°C, 420°C-900°C and above 950°C as shown in Table 4.2.

Table 4.2 The change in percent weight loss and energy of zinc waste

Temperature regions	Percent weight loss	Exothermic/Endothermic peak
100°C-190°C	8%wt	Exothermic
300°C-415°C	2%wt	Exothermic
420°C-900°C	4%wt	Endothermic
> 950°C	15%wt	Endothermic

It is observed from Fig.4.2 and Table 4.2 that in the temperature range of 100°C-190°C, an endothermic peak was found at ~ 150°C, resulting from the dehydration of gypsum ($\text{CaSO}_4 \cdot 2\text{H}_2\text{O}$). The 8% weight loss in this region indicates the evaporation of water. In the temperature range of 300°C-415°C, the weight loss was only ~2%, which exhibits the evaporation of trapped water in the structures. A small endothermic peak in this region was found at ~390°C, resulting from the transformation of anhydrite from soluble to insoluble. In the temperature range of 420°C-900°C, the weight was slowly declined, resulting in ~4% decrease. An exothermic peak was found at ~550°C. It is believed that the change in weight and the appearance of an exothermic peak in this region derive from the decomposition of a metal sulfate, such as iron sulfate which is then transformed to hematite (Fe_2O_3). At temperatures above 950°C, the weight rapidly decreased by ~15%, which was attributed to the melting of zinc waste (at ~1200°C).

Concerning to the decomposition of metal sulfate at 420°C-900°C, zinc waste had been calcined at 800°C for 2 hours to remove SO_2 prior to use for producing glasses.

4.1.3. Phase analysis

Zinc waste was calcined at six different temperatures, 300°C, 450°C, 600°C, 800°C, 1,150°C and 1,300°C, to investigate the phase change as the temperature increased, by XRD. Phase formation from XRD patterns of zinc waste at each temperature was then compared with phases that are existed in the original zinc waste. The XRD pattern of the original zinc waste is shown in Fig.4.3. While the XRD patterns of the waste calcined at 300 - 600°C and 800 - 1300°C are shown in are shown in Fig.4.4 and Fig.4.5, respectively.

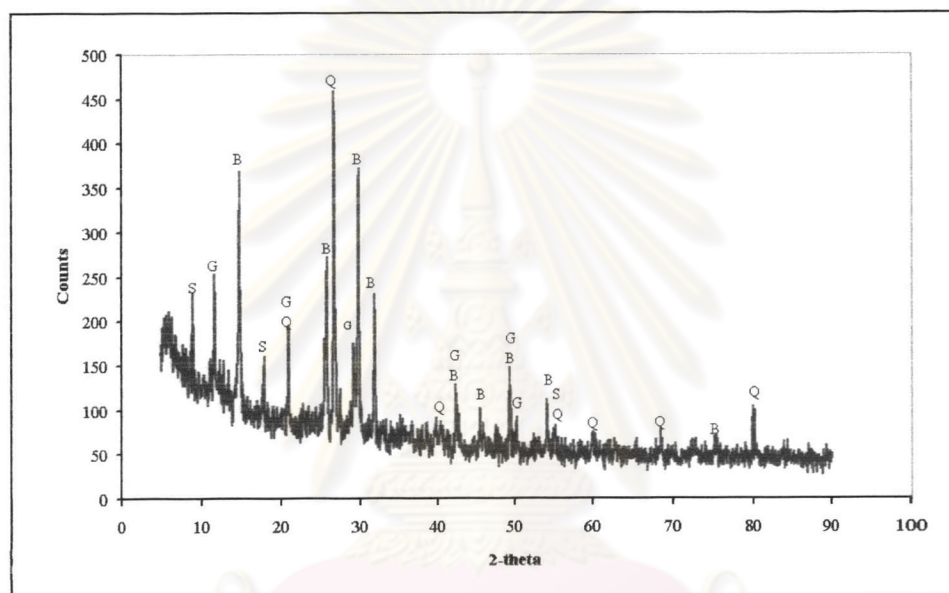


Fig. 4.3 XRD pattern of original zinc waste from Tak plant

Q: Quartz, B: Bassanite, G: Gypsum, S: Silicate

According to the XRD pattern, the original zinc waste, contained four major phases in zinc waste composition, which are quartz (SiO_2), gypsum ($\text{CaSO}_4 \cdot 2\text{H}_2\text{O}$), bassanite (β calcium sulfate hydrate: $\beta\text{-CaSO}_4 \cdot 2\text{H}_2\text{O}$) and phlogopite (potassium magnesium aluminum fluoride silicate: $\text{KMg}_3(\text{Si}_3\text{Al})\text{O}_{10}\text{F}_2$), with small amount of sulfur compounds such as copper sulfide (CuS), iron sulfate (FeSO_4) and zinc sulfate ($\text{ZnSO}_4 \cdot \text{H}_2\text{O}$).

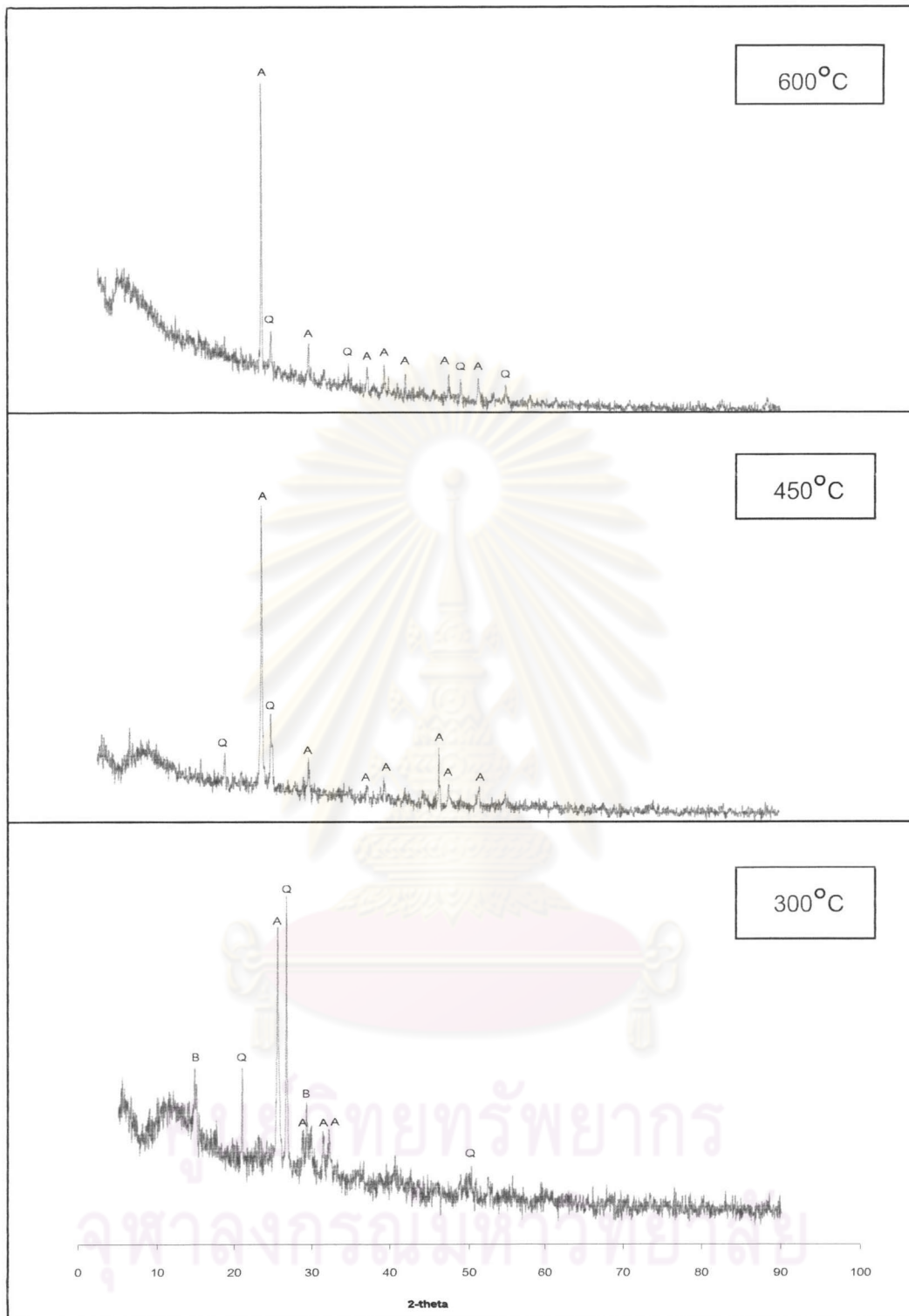


Fig. 4.4 XRD patterns of zinc waste calcined at 300°C, 450°C and 600°C

Q: Quartz, B: Bassanite, G: Gypsum, A: Anhydrite

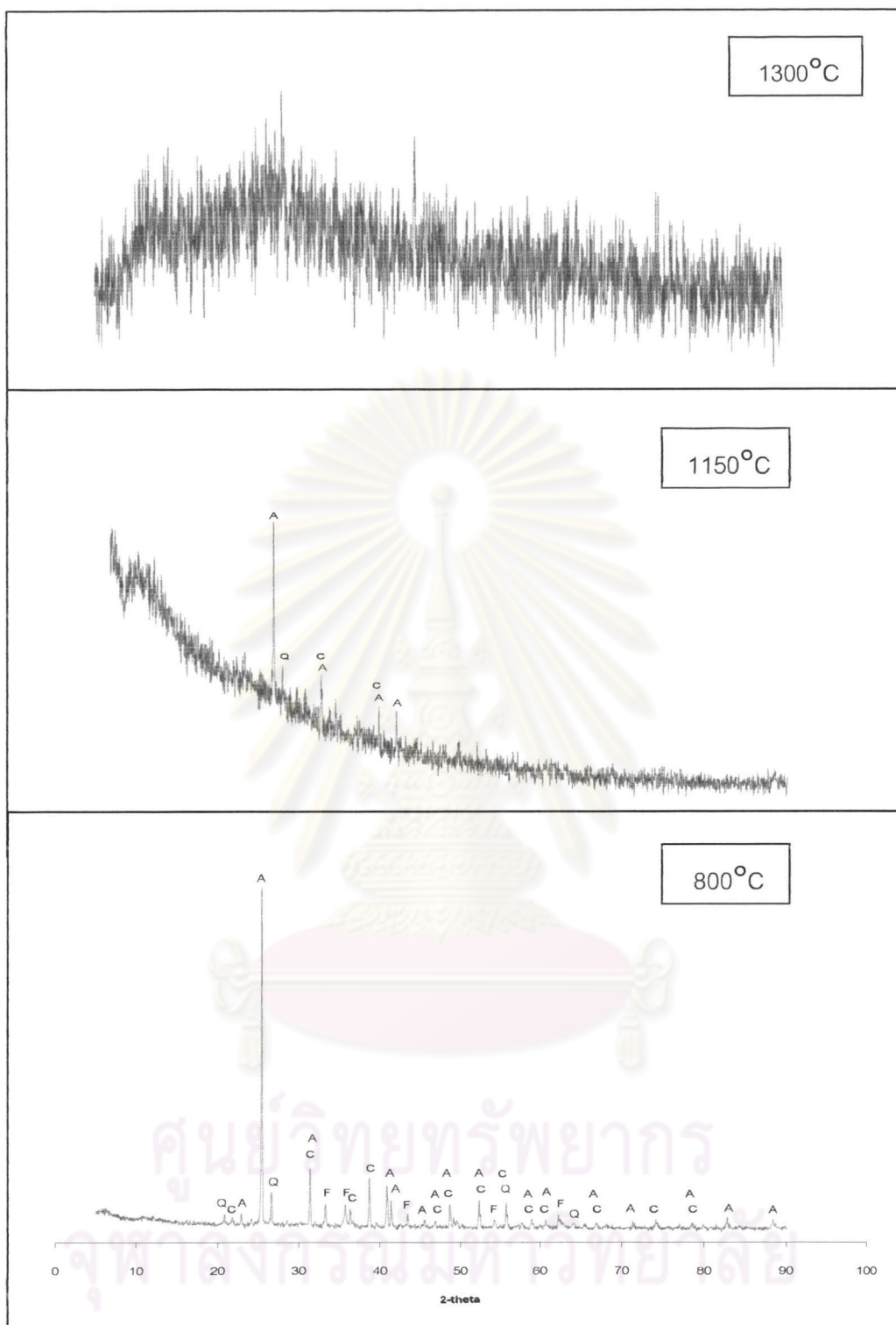


Fig. 4.5 XRD patterns of zinc waste calcined at 800°C, 1150°C and 1300°C

Q: Quartz, A: Anhydrite, C: Cristobalite, F: Hematite

Consider XRD pattern of zinc waste calcined at 300°C. Anhydrite or calcium sulfate (CaSO_4) was found as a new phase with low intensity of bassanite peaks. The lower in intensity of bassanite peaks indicates the evaporation of water molecules as the temperature increased.

At 450°C, the peaks of bassanite phase disappeared indicating that the water molecules were completely evaporated of from zinc waste. It was also observed that anhydrite has become a dominant phase (as shown in high intensity) with low intensity of quartz.

At 600°C, only two phases, anhydrite and quartz were observed with no new phase formation.

At 800°C, hematite (Fe_2O_3) and cristobalite (SiO_2) phases were found with low intensity. Anhydrite and quartz remained as stable phases.

At 1,150°C, three major phases were observed, which were anhydrite, cristobalite and quartz. Anhydrite phase remained dominant, although low with intensity. Hematite phase was absent at this temperature. Amorphous phase was observed as a mixed phase with other crystalline phases. The appearance of amorphous hump and the decreasing of crystalline phase intensities indicate the initial melting of zinc waste as the temperature increases close to its melting point.

At 1300°C, it is noticeable that the only phase shown was amorphous since no crystalline phase was observed.

Besides the change of phases as the temperature increased, the color of zinc waste had changed after calcining. The color change was considered together with the phase formation from the XRD patterns and TG/DTA curves. The original color of zinc waste from the Tak plant was yellow as shown in Fig.4.6 (a). At 300°C, the color changed to yellow-brown. At 450°C, the color changed to brown because of the completed evaporation of water molecules from the structures, which can be confirmed by the disappearance of bassanite phase in XRD pattern. At 600°C, the color changed

to red. The change of color to red was believed to be attributed to the formation of iron oxide (Fe_2O_3) with respect to TG/DTA results. At 800°C , the color changed to dark-red, which indicated the increasing of iron oxide phase formation with respect to both TG/DTA results and XRD pattern. It is noticeable that at 1150°C , zinc waste was partly melted as the powder was aggregated together after calcining.

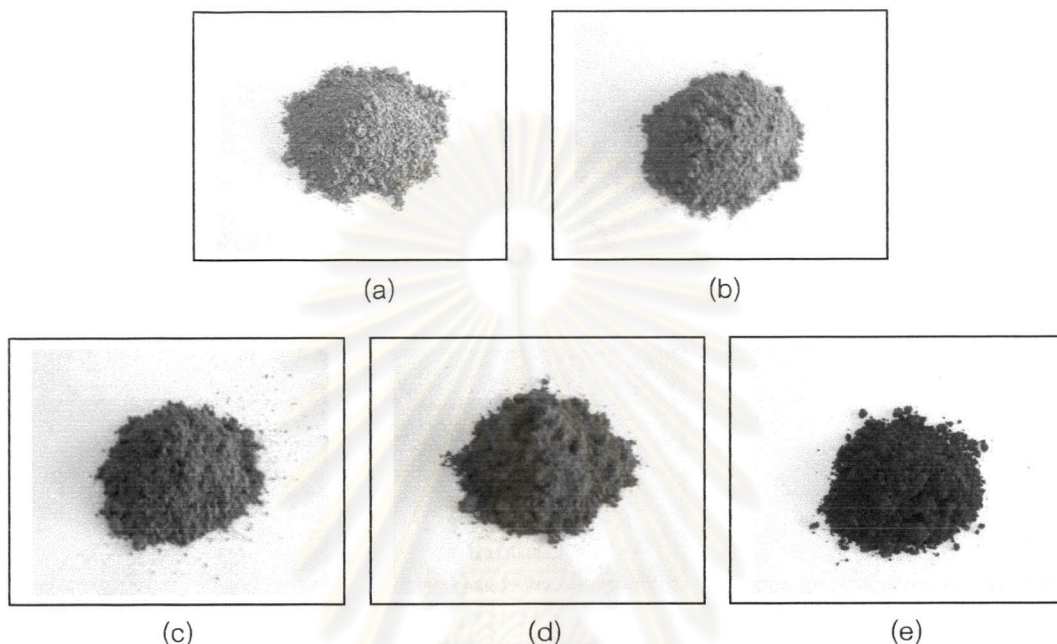


Fig. 4.6 Zinc waste from Tak plant (a) and zinc waste calcined at 300°C (b), 450°C (c), 600°C (d), 800°C (e)

4.1.4. Particle size distribution

Particle size distribution of zinc waste was examined by master sizer machine. Various sizes of particles were found in the range of $0.35\text{-}300\ \mu\text{m}$ as illustrated in a broad and wide curve of particle size distribution shown in Fig.4.7. The average particle size is $\sim 5\ \mu\text{m}$.

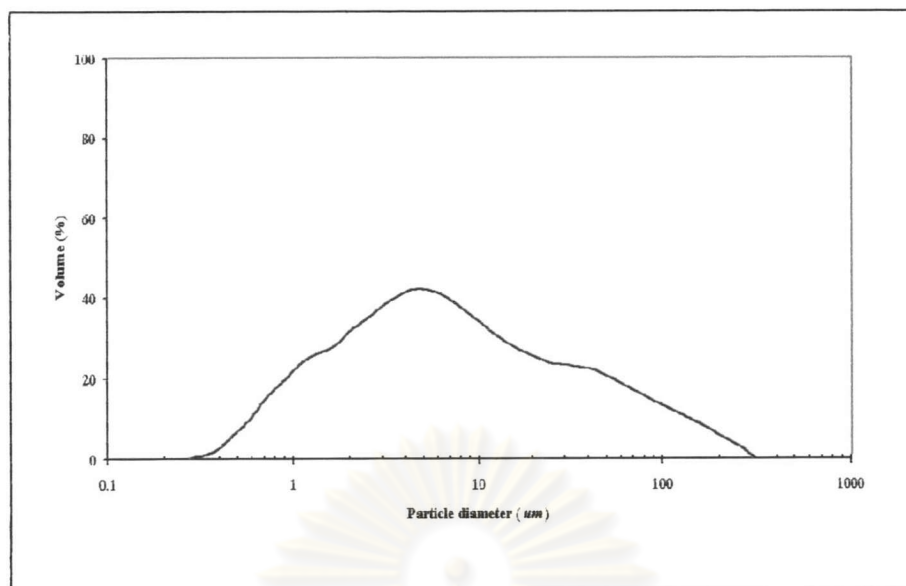


Fig. 4.7 Particle size distribution of zinc waste

4.1.5. Morphologies of zinc waste

Morphologies of zinc waste were investigated by SEM. The images of zinc waste particles are shown in Fig.4.8. Zinc waste contained various groups of small particles formed together in two different shapes. The groups of particles formed as large rod like grains are shown in Fig.4.8 (a) and those that formed as small irregular grains are shown in Fig.4.8 (b).

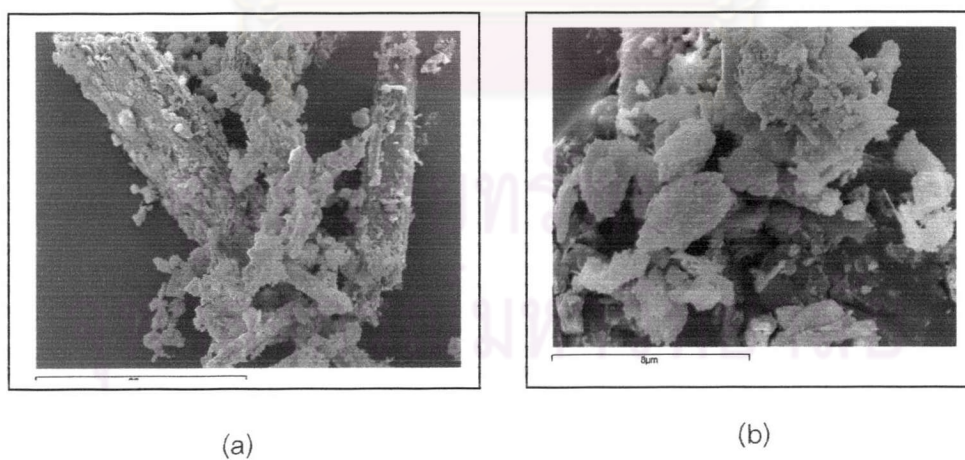


Fig. 4.8 SEM images of zinc waste as rod like grains (a) and irregular grains (b)

4.2 Characterization of melted glasses

4.2.1. Physical behavior

All the mixtures of twenty-five glasses were melted at $1,450^{\circ}\text{C}$ for 1 hour. After melting the glasses were investigated for their melting behavior (viscosity), homogeneity and color by visual observation and optical microscopy (OM). It was found that twenty-three out of twenty-five glasses were homogeneously melted without any remaining undissolved materials. Phase separation was observed in two glasses, which were G#13 and G#14. It was noticeable that during pouring the viscosity of the melted G#15 and G#19 were very high. This is because they contained high percentage of SiO_2 .

The images of melted glasses G#2, G#5, G#13, G#15 and G#24 are given as examples in Fig.4.9. The rest were shown in Fig.B-1 in Appendix B. It was observed that the glass with phase separation had blue-white appearance while the homogeneous glasses were black. It was also found that the shape of high viscosity glasses (G#15 and G#19) was distorted whereas others were in a good circular shape.

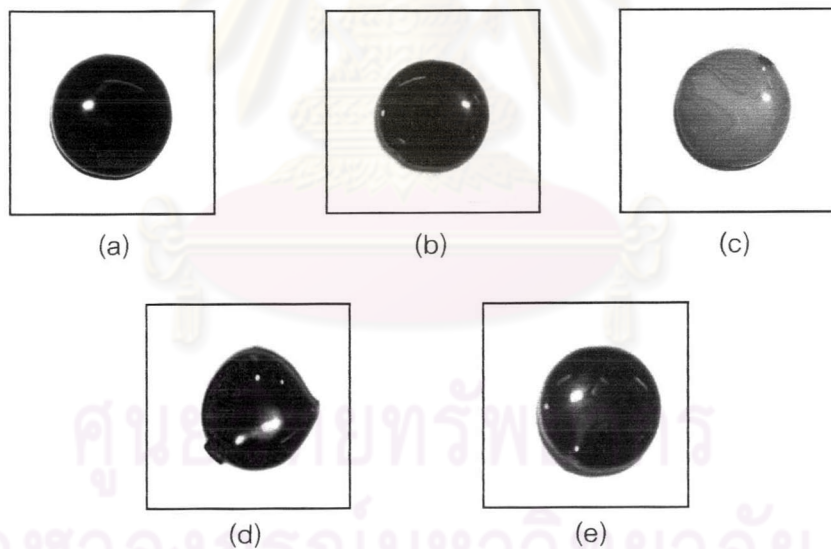


Fig. 4.9 Melted glasses of GC#2 (a), GC#5 (b), GC#13 (c), GC#15 (d), GC#24 (e)

The images of glasses taken by OM are shown in Fig.4.10. The images of homogeneous glasses, G#8 (a) and G#21 (b) were compared with the images of phase-

separated glasses G#13 (c) and G#14 (d). The phase-separated glasses were found to contain large amount of droplets distributed in the glass matrix.

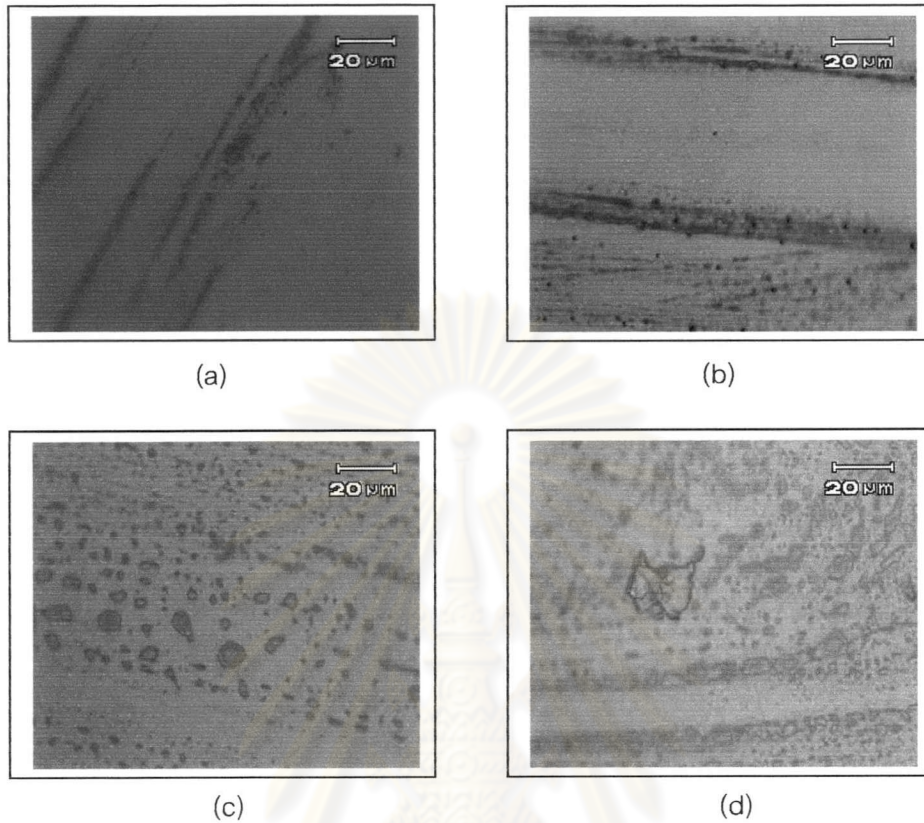


Fig. 4.10 OM images of melted glasses G#8 (a), G#10 (b), G#13 (c) and G#14 (d)

4.2.2. Thermal behavior

Prior to producing glass-ceramics, the glass transition temperature (T_g) and crystallization temperature (T_c) of the twenty-five glasses were examined by TG/DTA. The T_g and T_c can be observed from the deviation of DTA curve apart from a base line with exothermic peak. Therefore both T_g and T_c can be estimated by considering a point of intersection between a base line and a slope line of the first deviation curve. The estimation of T_g and T_c of G#13 was given as an example in Fig.4.11. One might find the endothermic peak at elevated temperature that demonstrates the values of melting of glass.

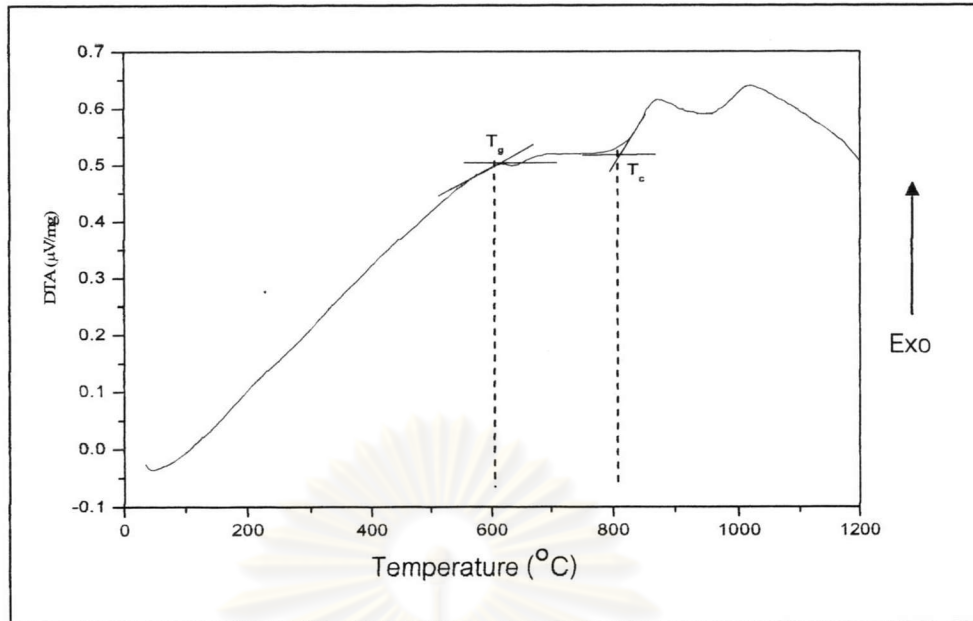


Fig.4.11 DTA curve of G#13

An exothermic peak of T_g and T_c can be seen in every DTA curve indicating that glasses would simply form glass-ceramics. It was found that T_g and T_c of the twenty-five glasses are in the range of 550°C - 630°C and 680°C - 870°C respectively. These temperature ranges were then used to design nucleation and crystallization temperatures in producing of glass ceramics. The values of T_g and T_c of twenty-five glasses were measured and summarized in Table 4.3.

ศูนย์วิทยทรัพยากร
จุฬาลงกรณ์มหาวิทยาลัย

Table 4.3 T_g and T_c of twenty-five glasses

G#	T_g ($^{\circ}\text{C}$) ± 5	T_c ($^{\circ}\text{C}$) ± 5	G#	T_g ($^{\circ}\text{C}$) ± 5	T_c ($^{\circ}\text{C}$) ± 5
1	570	705	14	608	822
2	565	730	15	630	872
3	575	710	16	633	816
4	585	711	17	567	756
5	600	747	18	589	733
6	576	710	19	578	778
7	550	731	20	561	716
8	555	727	21	600	778
9	554	683	22	556	722
10	600	783	23	550	711
11	567	700	24	561	722
12	600	738	25	605	794
13	600	805			

4.3 Characterization of glass-ceramics

Glass-ceramics were prepared by heat-treatment process in four different conditions: condition A (550°C for 1 hour and 650°C for 2 hours), condition B (650°C for 1 hour and 750°C for 2 hours), condition C (750°C for 1 hour and 850°C for 2 hours), condition D (850°C for 1 hour and 950°C for 2 hours) as described in table 3.5 (Chapter 3). The colors of glass-ceramics were changed after heat-treatment from black to various colors such as yellow, brown and green, depending on compositions of parent glasses and heat treatment temperatures.

4.3.1. Physical properties

After heat-treatment at condition A, B, C and D, various physical properties include bulk density, percent volume shrinkage, percent water absorption and percent apparent porosity were examined to evaluate the sintering behavior. The results were considered in three different groups that were classified by the sintering and the firing

characteristic of glass-ceramic specimens observed visually after heat treatment. Group 1 is a group of not well-sintered glass-ceramics consisted of GC#13, GC#14, GC#15, GC#17, GC#21 and GC#25. Group 2 is a group of well-sintered glass-ceramics consisted of GC#2, GC#3, GC#4, GC#5, GC#6, GC#7, GC#8, GC#10, GC#18, GC#19, GC#22, GC#23 and GC#24. Group 3 is a group of over-fired glass-ceramics consisted of GC#1, GC#9, GC#11, GC#12, GC#16 and GC#20. The not well-sintered glass-ceramics in group 1 are shown Fig.4.12.



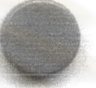








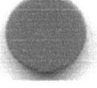












	Heat-treatment conditions			
	A	B	C	D
GC#13				
GC#14				
GC#15				
GC#17				
GC#21				
GC#25				

Fig.4.12 The not well-sintered glass-ceramics (group 1)

The variation of bulk density, percent volume shrinkage, percent water absorption and percent apparent porosity as a function of heat-treatment temperatures at condition A, B, C and D of glass-ceramics group 1 are shown in Fig.4.13, Fig.4.14, Fig.4.15 and Fig.4.16, respectively.

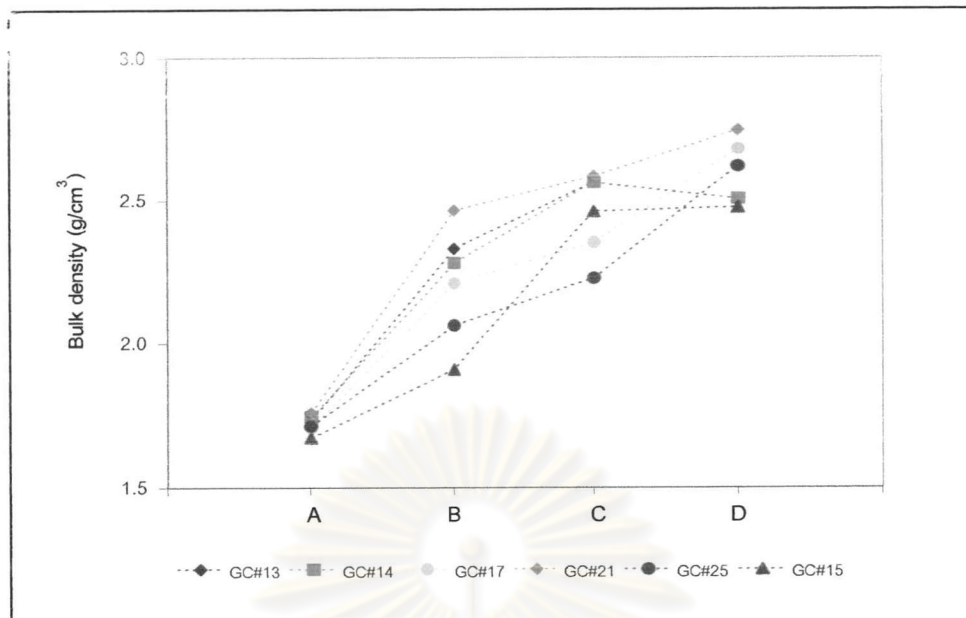


Fig.4.13 Bulk density of not well-sintered glass-ceramics (group 1)

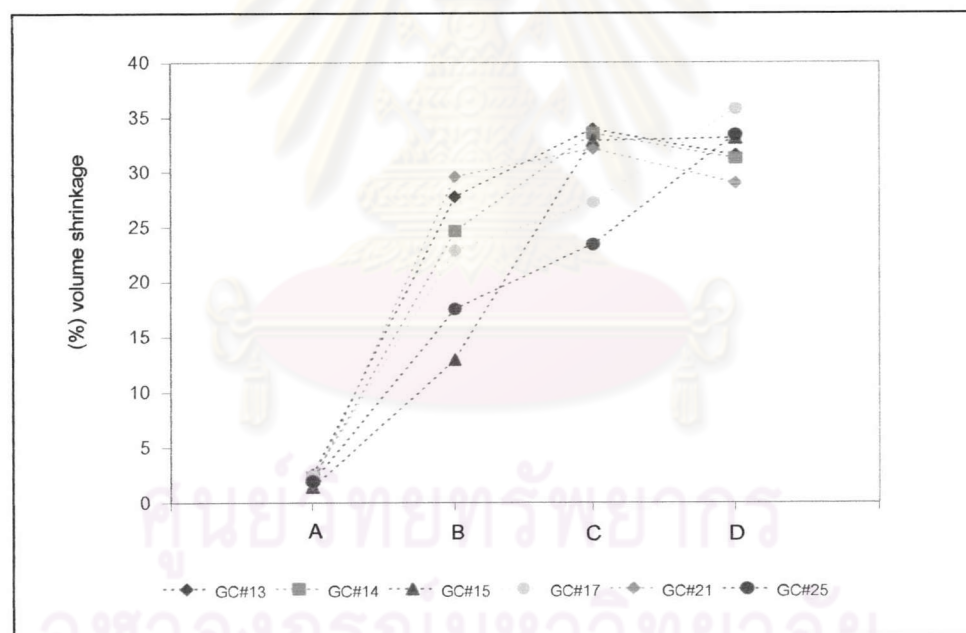


Fig.4.14 Percent volume shrinkage of not well-sintered glass-ceramics (group 1)

Bulk density and percent volume shrinkage increased with the increasing of heat-treatment temperatures.

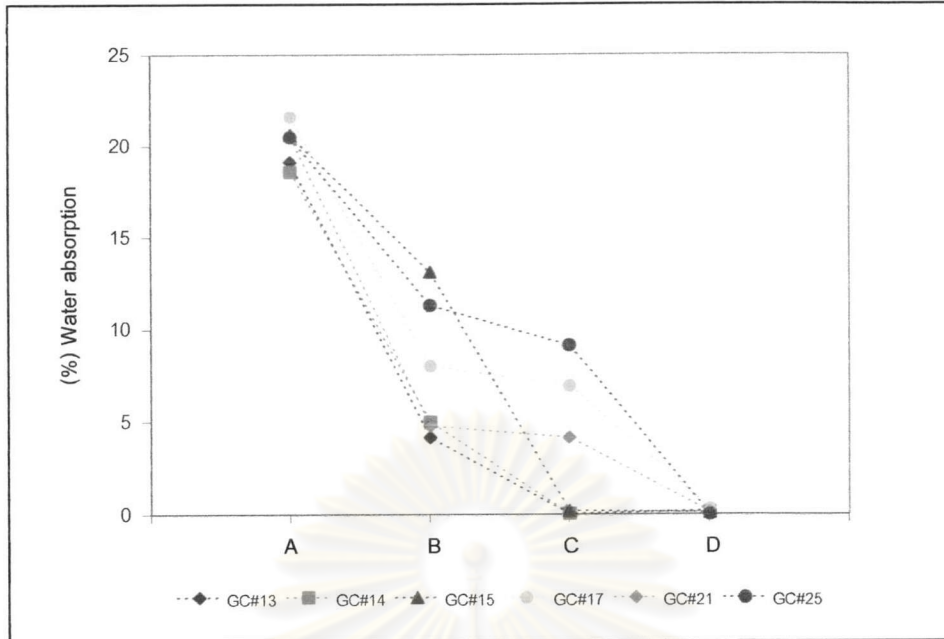


Fig. 4.15 Percent water absorption of not well-sintered glass-ceramics (group 1)

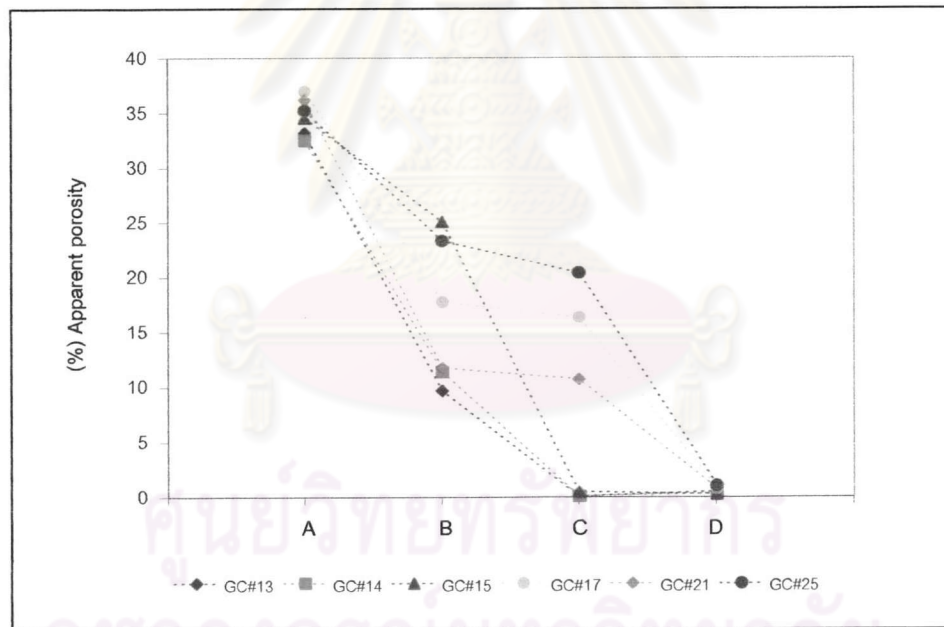


Fig.4.16 Percent apparent porosity of not well-sintered glass-ceramics (group 1)

Percent water absorption and percent apparent porosity decreased with the increasing of heat-treatment temperatures. After heat-treatment at condition C and D, percent water absorption and percent apparent porosity decreased to ~0%.

The specimens of the well-sintered glass-ceramics in group 2 are shown in Fig.4.17. The specimens are in the good circular shape after heat-treatment


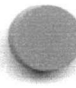



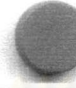
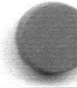
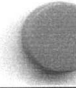



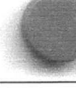


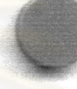



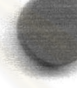


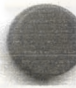









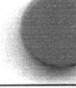







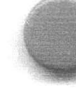












	Heat-treatment conditions			
	A	B	C	D
GC#2				
GC#3				
GC#4				
GC#5				
GC#6				
GC#7				
GC#8				
GC#10				
GC#18				
GC#19				
GC#22				
GC#23				
GC#24				

Fig.4.17 The well-sintered glass-ceramics (group 2)

The variation of bulk density, percent volume shrinkage, percent water absorption and percent apparent porosity as a function of heat-treatment temperatures at condition A, B, C and D of glass-ceramics group 2 are shown in Fig.4.18, Fig.4.19, Fig.4.20 and Fig.4.21, respectively.

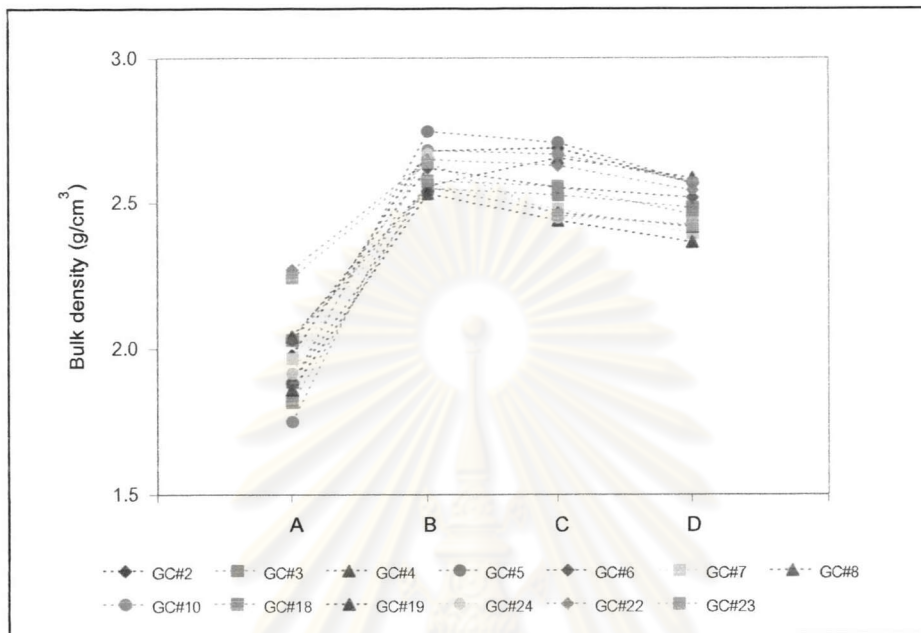


Fig.4.18 Bulk density of well-sintered glass-ceramics (group 2)

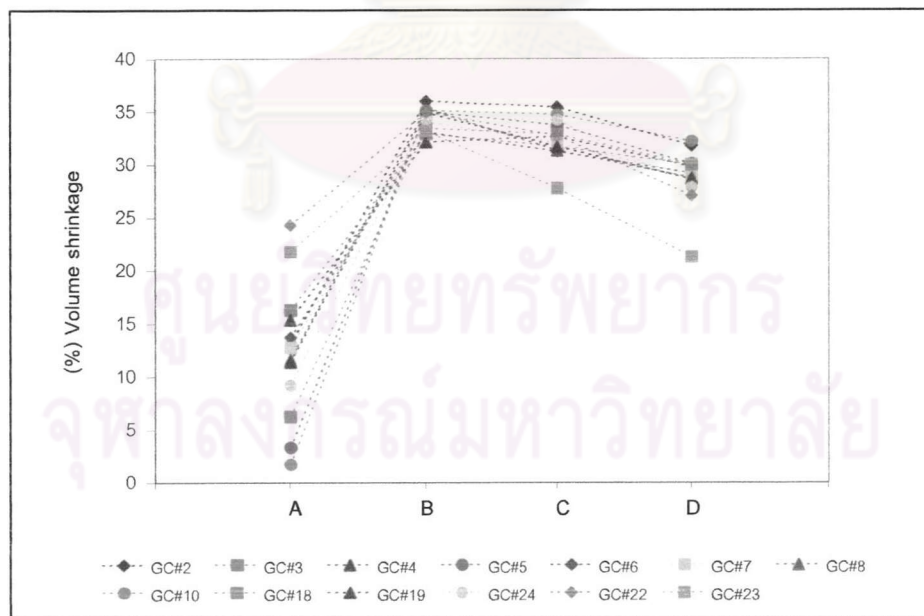


Fig.4.19 Percent volume shrinkage of well-sintered glass-ceramics (group 2)

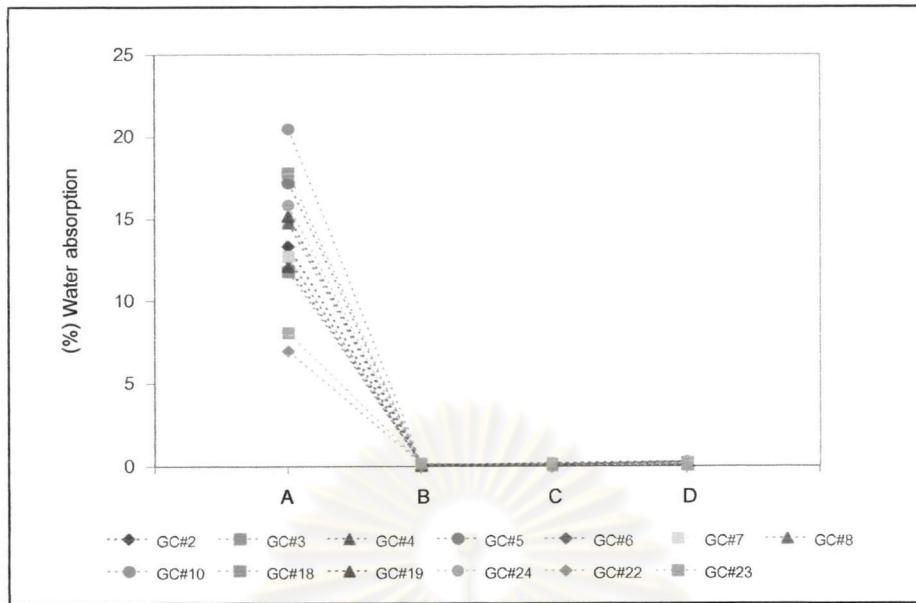


Fig.4.20 Percent water absorption of well-sintered glass-ceramics (group 2)

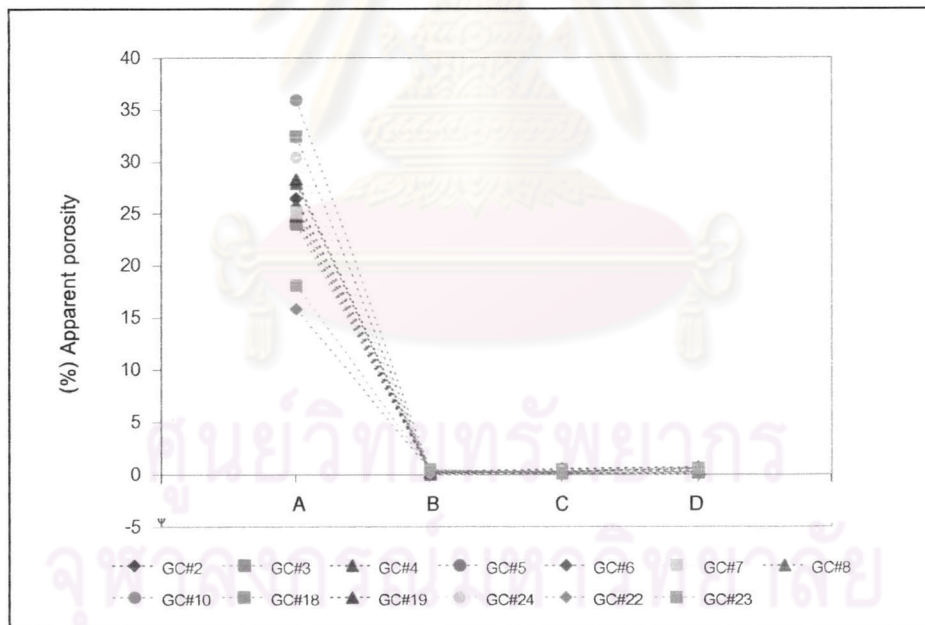


Fig.4.21 Percent apparent porosity of well-sintered glass-ceramics (group 2)

Bulk density and percent volume shrinkage increased with the increasing of heat-treatment temperatures after heat-treatment at condition A and B. On the other hand, bulk density and percent volume shrinkage slightly decreased with the increasing of heat-treatment temperatures after heat-treatment at condition C and D. Percent water absorption and percent apparent porosity decreased with the increasing of heat-treatment temperatures. Percent water absorption and percent apparent porosity decreased to ~0% after heat-treatment at condition B, C and D.

The over-fired glass-ceramic specimens in group 3 are shown in Fig.4.22. The specimens were in a good circular shape after heat-treatment at condition A, and B whereas many bloated after heat-treatment at condition C and D.

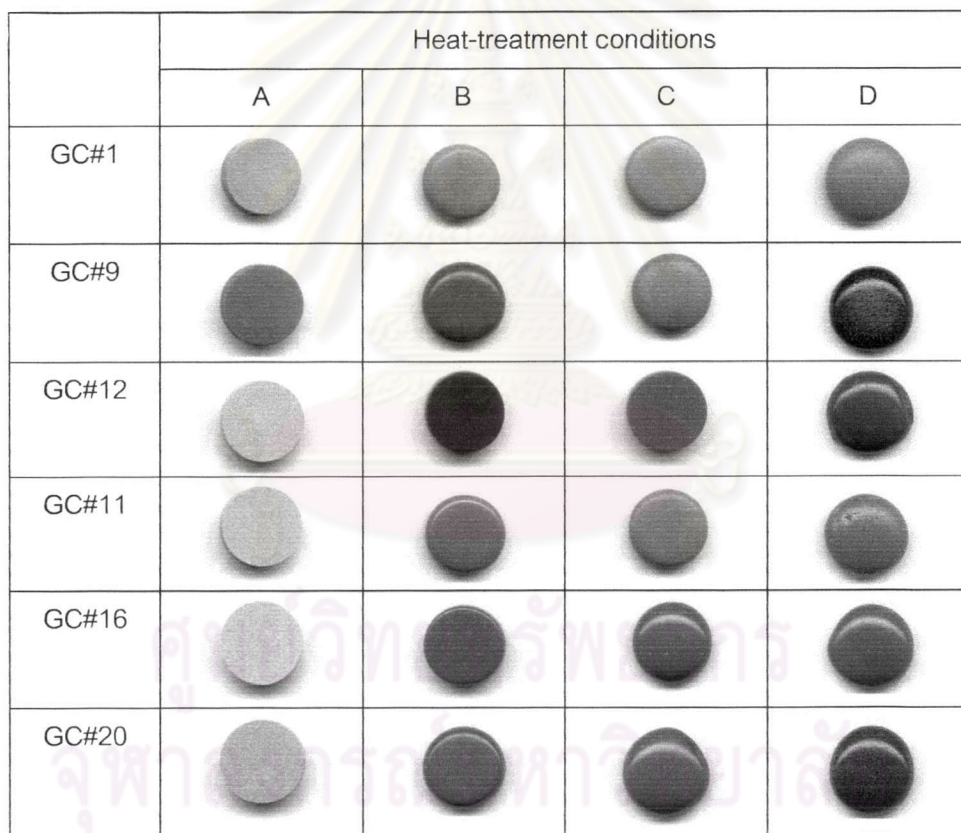


Fig.4.22 The over-fired glass-ceramic specimens (group 3)

The variation of bulk density, percent volume shrinkage, percent water absorption and percent apparent porosity as a function of heat-treatment temperatures

at condition A, B, C and D of glass-ceramics group 3 are shown in Fig.4.23, Fig.4.24, Fig.4.25 and Fig.4.26, respectively.

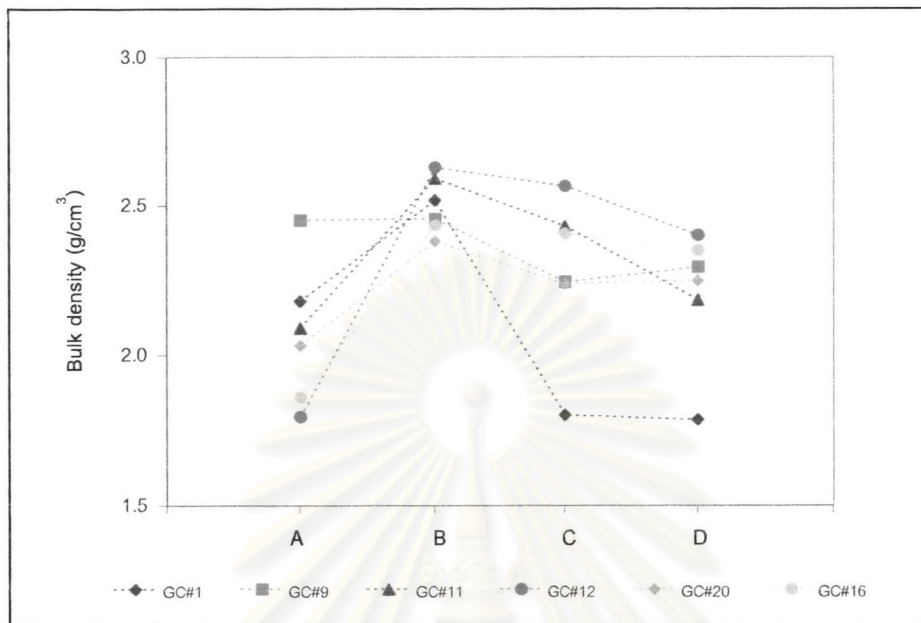


Fig.4.23 Bulk density of over-fired glass-ceramics (group 3)

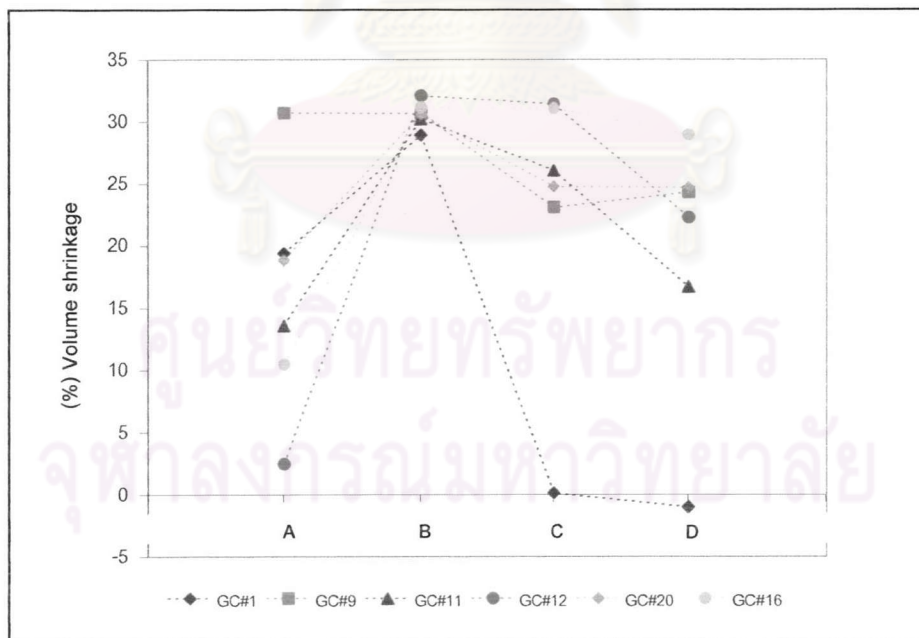


Fig.4.24 Percent volume shrinkage of over-fired glass-ceramics (group 3)

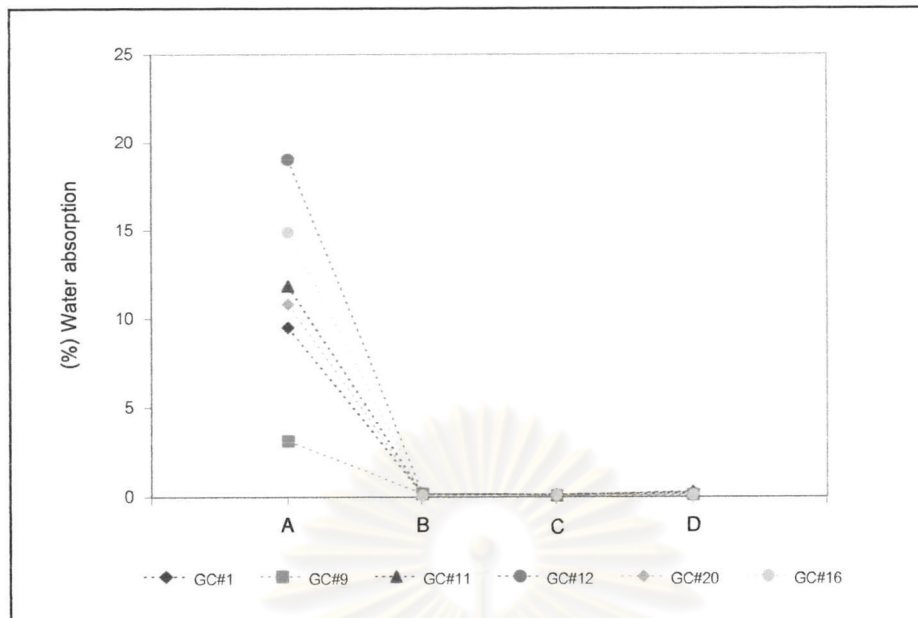


Fig.4.25 Percent water absorption of over-fired glass-ceramics (group 3)

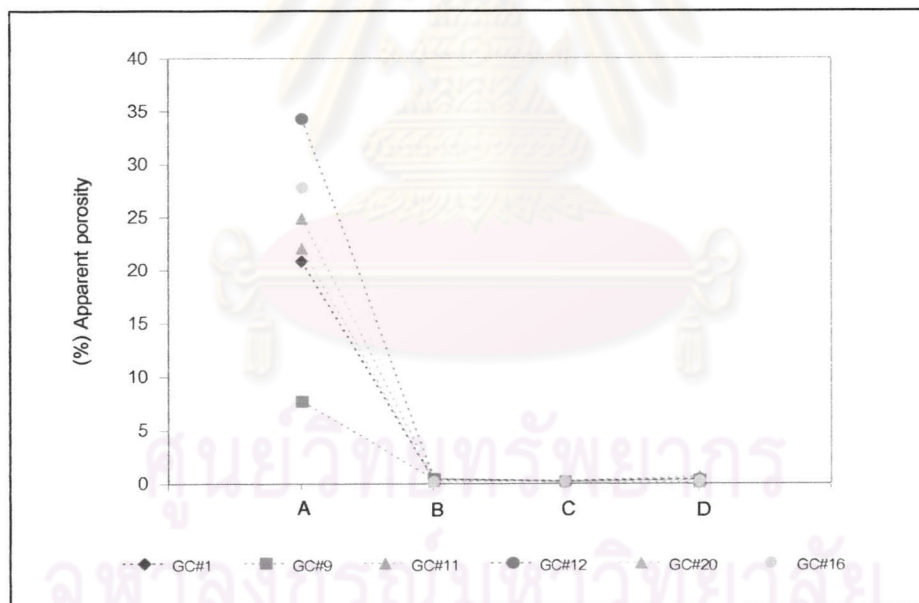


Fig.4.26 Percent apparent porosity of over-fired glass-ceramics (group 3)

Bulk density and percent volume shrinkage increased with the increasing of heat-treatment temperatures after heat-treatment at condition A and B whereas they

intensely decreased with the increasing of heat-treatment temperatures after heat-treatment at condition C and D. Percent water absorption and percent apparent porosity decreased with the increasing of heat-treatment temperatures. Percent water absorption and percent apparent porosity decreased to ~0% after heat-treatment at condition B, C and D.

Basically, the density is an intensive property and is the relative between mass and volume of the substances. Bulk density, in terms of glass-ceramics, is an additive function of the volume fraction of the glass and crystal phases co-existing in glass-ceramics. Percent volume shrinkage indicates the final-shape of glass-ceramics after heat-treatment. A product is commonly referred to as over firing if a reduced shrinkage was observed. Percent water absorption is proportional to percent apparent porosity. Percent apparent porosity indicates the percent of opened pores-those pores connected to the surface. During the heat-treatment process some open pores are eliminated directly, many are transformed into closed pores. As a result, the volume fraction of closed pores increases initially and only decreases toward the end of the firing process. For maximizing properties such as strength, translucency, and thermal conductivity, it is desirable to eliminate as much of porosity as possible [9].

Therefore, in order to evaluate the sintering behavior, all of these properties were considered. It is noticeable that bulk density and percent volume shrinkage of the unwell-sintered glass-ceramics group 1 were very low after heat-treatment at condition A and B. When considering together with percent water absorption and percent apparent porosity, high percentage of water absorption and apparent porosity was observed. This demonstrates the not-sintered characteristic as the remaining of opened pores. Bulk density of the over-fired glass-ceramics group 3 intensely decreased after heat-treatment at condition C and D as well as percent volume shrinkage indicating the over-fired characteristic. Since it is believed that the decreasing of percent water absorption and percent apparent porosity after heat-treatment is a consequence of the elimination of opened pores. Therefore the opened pores of the unwell-sintered glass-ceramics group 1 were almost completely removed after heat-treatment at condition C and D, as the percent water absorption and percent apparent porosity decreased to ~0%,

whereas the opened pores of the well-sintered glass-ceramics group 2 and the over-fired glass-ceramics group 3 were almost completely removed after heat-treatment at condition B, C and D. The well-sintered glass-ceramics group 2 seemed to offer good physical properties after heat-treatment at condition B, C and D.

The raw data of percent volume shrinkage, bulk density, percent water absorption and percent apparent porosity after heat-treatment at condition A, B, C and D are shown in Table C-1, Table C-2, Table C-3 and Table C-4 in Appendix C, respectively. Bulk density of twenty-five glass-ceramics after heat-treatment at condition A, B, C and D were in the range of 1.71-2.45 g/cm³, 1.91-2.74 g/cm³, 1.80-2.71 g/cm³, 1.78-2.75 g/cm³, respectively.

In terms of heat-treatment temperature, most of glass-ceramics were not well-sintered after heat-treatment at condition A whereas glass-ceramics were mostly over fired after heat-treatment at condition D. This indicates that the heat treatment process at condition A and D were not suitable for producing glass-ceramics in this study. Therefore glass-ceramics derived from heat-treatment process at conditions B and C were selected for the further characterization.

4.3.2. Crystal phase formation

Crystalline phases of glass-ceramics heat-treated at condition B (650°C for 1 hour and 750°C for 2 hours) and condition C (750°C for 1 hour and 850°C for 2 hours) were identified by XRD. The size and morphology of crystals were observed by SEM. Chemical compositions of the crystals and residual glass were determined by EDS. Five major crystal phases were found in glass-ceramics as a single phases: wollastonite-ferroan ($\text{Ca}_{2.87}\text{FeO}_{0.13}(\text{SiO}_3)_3$), pyroxene ($\text{Mg}_{0.937}\text{Fe}_{0.063}(\text{Ca}_{0.75}\text{Na}_{0.249}\text{Fe}_{0.018})(\text{Si}_2\text{O}_6)$), anorthite ($\text{Ca}(\text{Al}_2\text{SiO}_8)$), quartz (SiO_2), and cristobalite (SiO_2). Multiple phases resulting from the mixing of the above crystal phases were also found in a number of glass-ceramics such as the mixed phases of wollastonite-ferroan and anorthite, the mixed phases of quartz and cristobalite and the mixed phases of quartz, cristobalite and anorthite. Crystal phase formation can be affected by the compositions of each glass-ceramic and the heat-treatment temperatures. The results were discussed by

considering the correlation of glass-ceramic compositions and heat-treatment temperature of single phase formation and multiple phase formation as follows:

- **Single phase formation**

- 1. Wollastonite-ferroan crystalline phase**

The single wollastonite-ferroan phase was found in GC#1, GC#10, GC#23 and GC#24. The compositions of these glass-ceramics enriched of CaO with medium amount of SiO₂ as shown in Table 4.4.

Table 4.4 Compositions of glass-ceramics contained wollastonite-ferroan phase

GC#	SiO ₂	B ₂ O ₃	Na ₂ O	CaO	MgO	ZnO	Al ₂ O ₃	Fe ₂ O ₃
1	45	15	15	20	0	1	1	3
10	57	5	5	20	0	3	5	5
23	55	5	15	18	0	1	1	5
24	55	5	13	20	0	1	1	5

The crystal formation of wollastonite-ferroan of GC#24 heat-treated at condition B and C was investigated by XRD, SEM and EDS techniques. The XRD patterns of GC#24 after heat-treatment at condition B and C are shown in Fig.4.27. The SEM micrographs after heat-treatment at condition B and C are shown in Fig.4.28 (a) and (b), respectively.

ศูนย์วิทยทรัพยากร
จุฬาลงกรณ์มหาวิทยาลัย

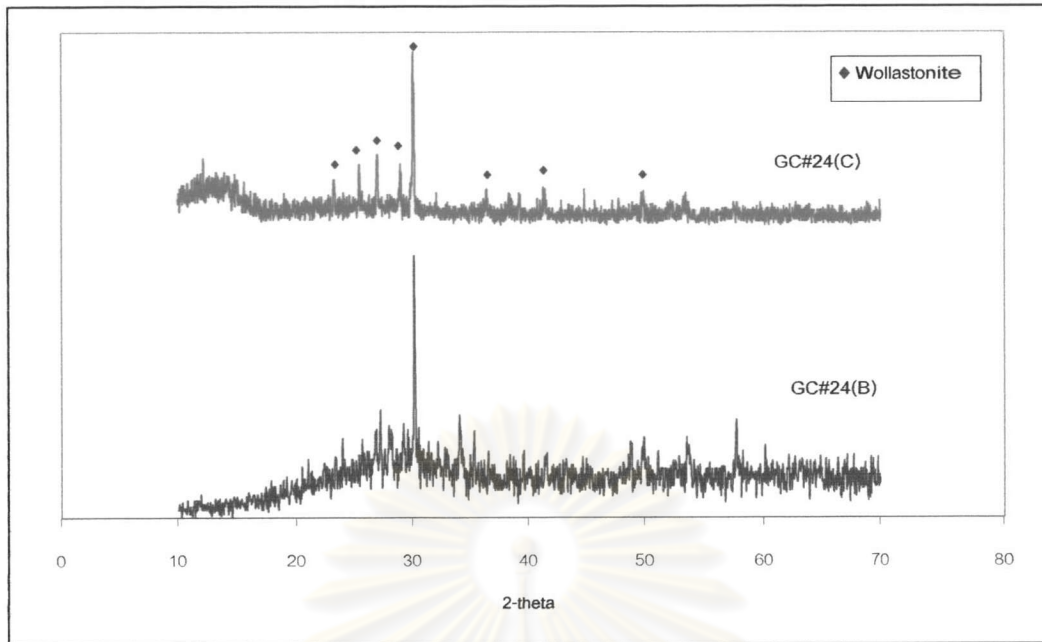


Fig.4.27 XRD patterns of GC#24 heat-treated at condition B and C

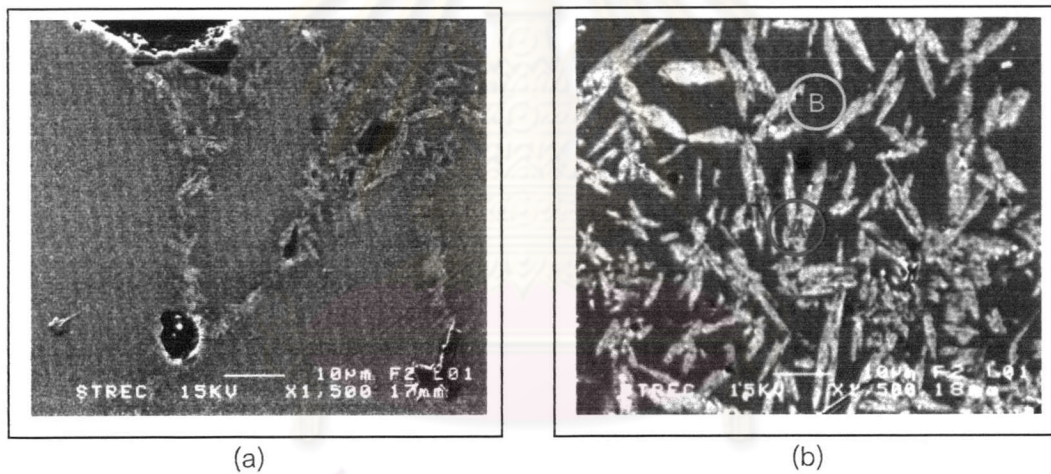


Fig.4.28 SEM micrographs (1500x) of wollastonite-ferroan phase observed in GC#24 at heat-treated at condition B (a) and C (b)

The crystalline peaks of wollastonite-ferroan of GC#24 were obviously seen in the XRD pattern after heat-treatment at condition B. Small acicular crystals dispersed in the glassy matrix were observed in the SEM micrograph after heat-treatment at condition B confirming the presence of wollastonite-ferroan. The crystalline peaks of wollastonite-ferroan as shown in the XRD pattern became narrower and sharper after heat-treatment

at condition C. The crystal size of wollastonite-ferroan noticeably increased after heat-treatment at condition C as can be seen from the SEM micrograph. The EDS spectrums, spotted on the acicular crystal area (A) and glassy matrix area (B), of GC#24 heat-treated at condition C are shown in Fig.D-1 and Fig.D-2 in Appendix D, respectively. The EDS analysis showed that acicular crystals contain mainly Si, Ca and confirming wollastonite-ferroan ($\text{Ca}_{2.87}\text{FeO}_{0.13}(\text{SiO}_3)_{3/3}$), as identified by XRD technique whereas the glassy matrix enriched in Si, Al, Na and Fe with poor in Ca.

The XRD patterns of GC #1 heat-treated at condition B and C are shown in Fig.D-3 in Appendix D. The XRD patterns and the SEM micrographs of GC #10 heat-treated at condition B and C are shown in Fig.D-4 and Fig.D-5 (a) and (b). The XRD patterns and the SEM micrographs of GC #23 heat-treated at condition B and C are shown in Fig.D-6 and Fig.D-7 (a) and (b).

2. Pyroxene crystalline phase

The single pyroxene phase was found in GC#2, GC#3, GC#5, GC#6, GC#17, GC#18, GC#21, GC#22, and GC#25 after heat-treatment at condition B and C. The pyroxene phase was found in glass-ceramics contained MgO as shown in Table 4.5.

Table 4.5 Compositions of glass-ceramics contained pyroxene phase

GC#	SiO ₂	B ₂ O ₃	Na ₂ O	CaO	MgO	ZnO	Al ₂ O ₃	Fe ₂ O ₃
2	55	5	15	10	10	1	1	3
3	45	15	11	10	10	1	5	3
5	45	15	5	18	10	3	1	3
6	45	15	11	10	10	3	1	5
17	56	5	5	15	10	1	5	3
18	45	15	10	10	9	1	5	5
21	56	5	5	15	10	3	1	5
22	55	5	15	10	8	1	1	5
25	55	5	5	20	8	3	1	3

The XRD patterns of GC#2 heat-treated at condition B and C are shown in Fig.4.29. The microstructures of GC#2 heat-treated at condition B and C are shown in Fig.4.30 (a) and (b), respectively.

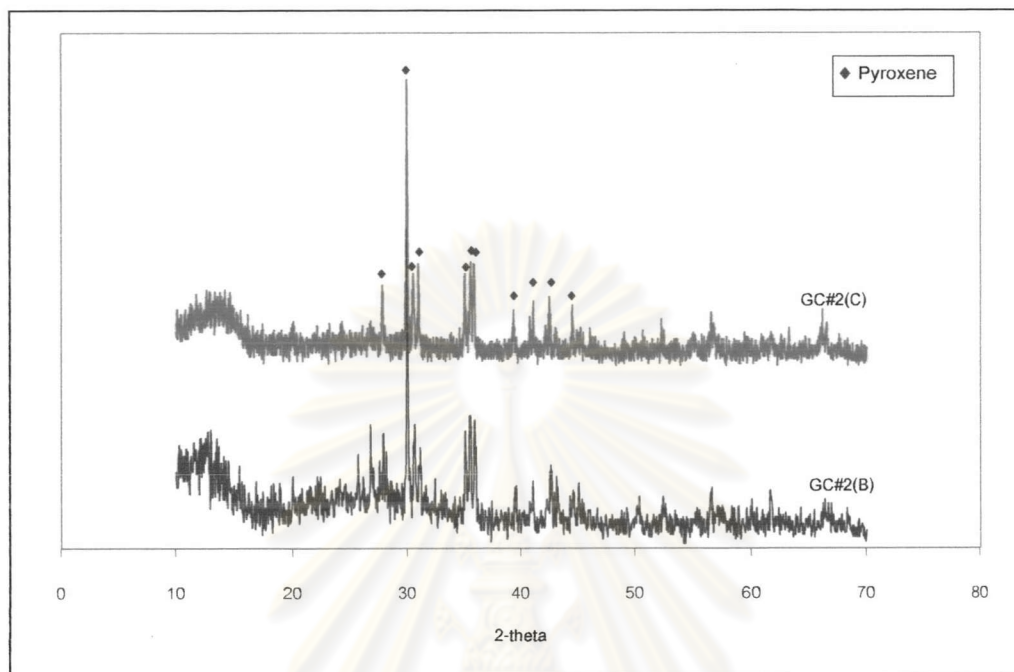


Fig.4.29 XRD patterns of GC#2 heat-treated at condition B and C

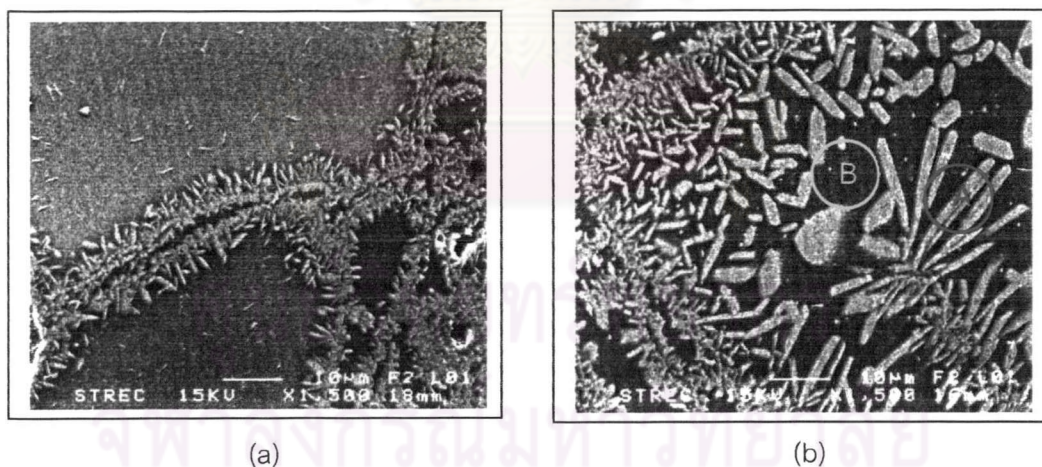


Fig.4.30 SEM micrographs (1500x) of pyroxene phase observed in GC#2 after heat-treatment at condition B (a) and C (b)

The crystalline peaks of pyroxene of GC#2 were obviously seen in the XRD pattern after heat-treatment at condition B. Small dendritic crystals dispersed in the glassy matrix were observed in the SEM micrograph after heat-treatment at condition B confirming the presence of pyroxene. The crystalline peaks of pyroxene as shown in the XRD pattern became narrower and sharper after heat-treatment at condition C. The crystal size of pyroxene noticeably increased after heat-treatment at condition C as can be seen from the SEM micrograph. The EDS spectrums, spotted on the dendritic crystal area (A) and glassy matrix area (B), of GC#2 heat-treated at condition C are shown in Fig.D-8 and Fig.D-9 in Appendix D, respectively. The EDS analysis showed that the dendritic crystals contain mainly Si, Mg, Ca and Fe confirming pyroxene $(Mg_{0.937}Fe_{0.063})(Ca_{0.75}1Na_{0.249}Fe_{0.018})(Si_2O_6)$, as identified by XRD technique whereas the glassy matrix enriched in Si, Al, Na with poor in Ca and Mg.

The XRD patterns and SEM micrographs of GC #3 after heat-treatment at condition B and C are shown in Fig.D-10 and Fig.D-11 (a) and (b). The XRD patterns and SEM micrographs of GC #5 after heat-treatment at condition B and C are shown in Fig.D-12 and Fig.D-13 (a) and (b). The XRD patterns GC #6, GC #17, GC #18, GC #21 and GC #22 are shown in Fig.D-14 - Fig.D-18, respectively. The XRD patterns and SEM micrographs of GC #25 after heat-treatment at condition B and C are shown in Fig.D-19 and Fig.D-20 (a) and (b).

3. Cristobalite crystalline phase

The single cristobalite phase was found GC#13 and GC#14, which were identically controlled. These glass-ceramics contained very high percentage of SiO_2 as shown in Table 4.6.

Table 4.6 Compositions of glass-ceramics contained cristobalite phase

GC#	SiO_2	B_2O_3	Na_2O	CaO	MgO	ZnO	Al_2O_3	Fe_2O_3
13	60	15	5	15	0	1	1	5
14	60	15	5	15	0	1	1	5

The XRD patterns and the SEM micrographs of GC#13 heat-treated at condition B and C are shown in Fig.4.31 and Fig.4.32 (a) and (b), respectively.

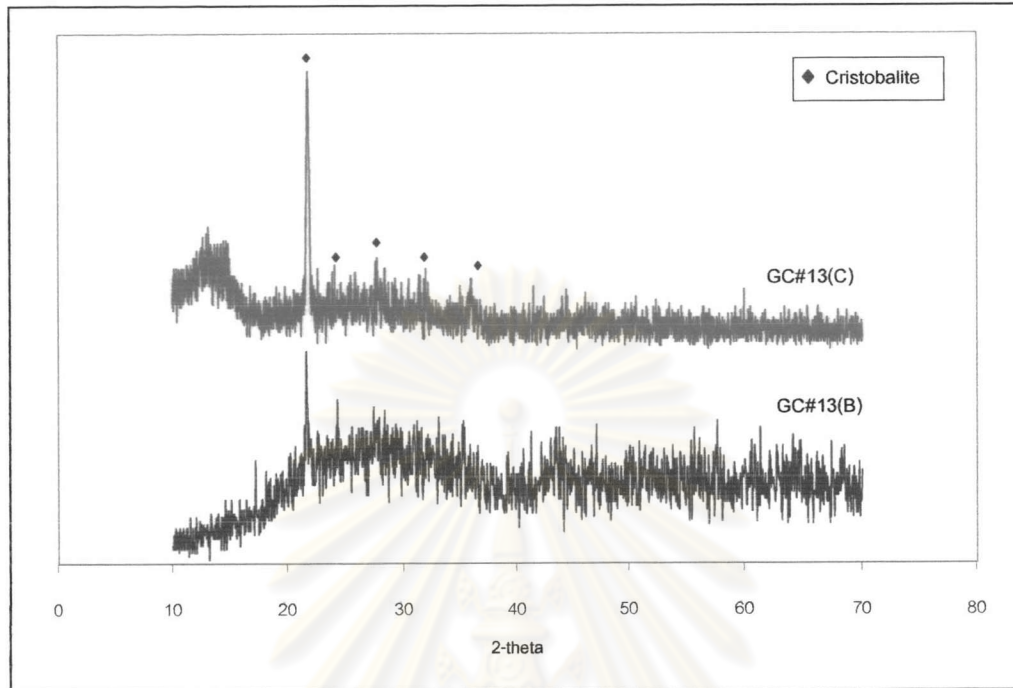


Fig.4.31 XRD patterns of GC#13 heat-treated at condition B and C

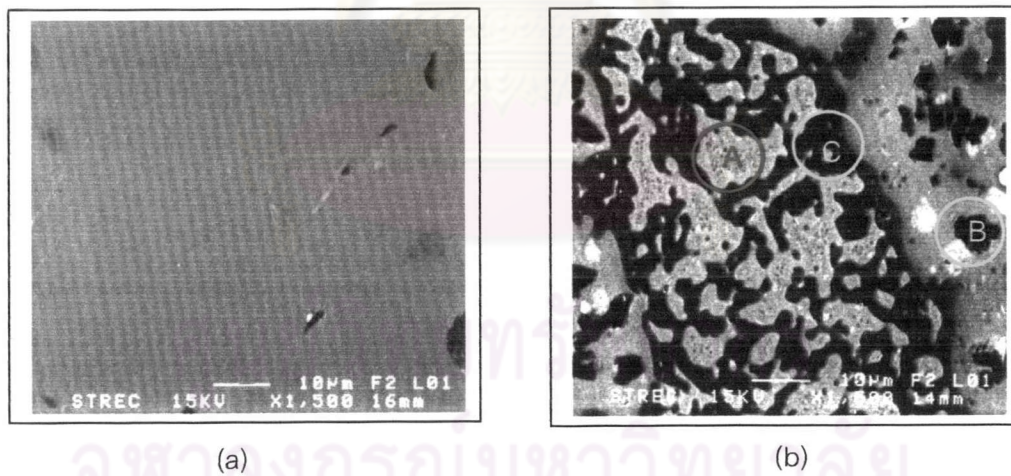


Fig.4.32 SEM micrographs (1500x) of cristobalite phase observed in GC#13 after heat-treatment at condition B (a) C (b)

The crystalline peaks of cristobalite were observed with an amorphous hump as shown in the XRD pattern after heat-treatment at condition B. A few of very small crystals dispersed in the glassy matrix were observed in SEM micrograph after heat-treatment at condition B confirming the crystallization. The narrow and sharp crystalline peaks of cristobalite can be clearly seen in the XRD pattern after heat-treatment at condition C. The crystal morphology of cristobalite can not be identified from the SEM micrograph, since the interconnected phases formed after heat-treatment at condition C. By visual observation, three different areas were observed including area (A), area (B) and area (C). The compositions of these areas were examined by EDS. The EDS spectrums, spotted on area (A), area (B) and area (C), of GC#13 heat-treated at condition C, are shown in Fig.D-21, Fig.D-22 and Fig.D-23 in Appendix D, respectively. The EDS analysis shows that the area (A) contains mainly Si and Ca whereas no significant differences between the compositions of area (B) and area (C) were observed. The area (B) and (C) contain great content of Si with less content of Ca when compared with area (A).

The XRD patterns and SEM micrographs of GC #14 after heat-treatment at condition B and C are shown in Fig.D-24 and Fig.D-25 (a) and (b). Since the compositions of GC#14 and GC#13 were identically controlled, the crystal phase formation and the microstructures of GC#14 were identically observed. It was believed that the characteristic the interconnected phases, observed from SEM micrographs of GC#13 and GC#14 after heat-treatment at condition C, indicates the microstructure of the spinodally decomposes glass, which is a type of phase-separated glass. The phase-separation in glass includes nucleated phase separation (crystallization) and the spinodal decomposition. The primary difference of the spinodal decomposition from nucleated phase separation is the interconnected, worm like morphology, which has been observed in many experiments [9, 10].

- Multiple phases

1. Mixed phases of wollastonite-ferroan and anorthite

The mixed phases of wollastonite-ferroan and anorthite phase were found in GC#4, GC#9, GC#11 and GC#12. These glass-ceramics contained low percentage of SiO_2 and high percentage of CaO as shown in Table 4.7.

Table 4.7 Compositions of glass-ceramics contained mixed phases of wollastonite ferroan and anorthite

GC#	SiO_2	B_2O_3	Na_2O	CaO	MgO	ZnO	Al_2O_3	Fe_2O_3
4	45	15	11	20	0	1	5	3
9	47	15	5	20	0	3	5	5
11	45	15	13	20	0	3	1	3
12	47	15	15	10	0	3	5	5

The XRD patterns of GC#4 heat-treated at condition B and C are shown in Fig.4.33. The microstructures of GC#4 heat-treated at condition B and C are shown in Fig.4.34 (a) and (b), respectively.

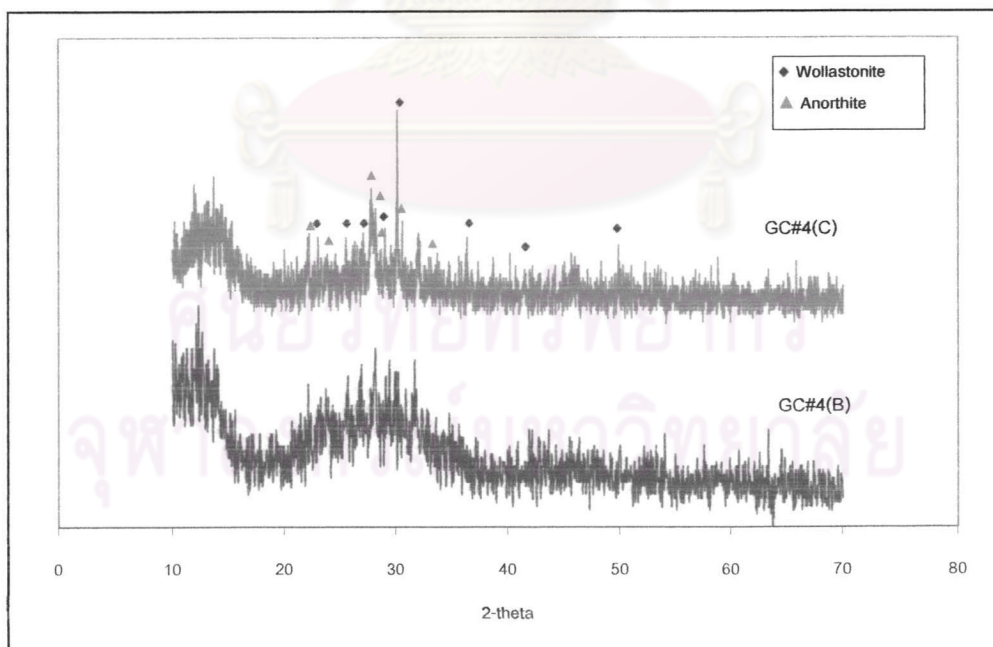


Fig.4.33 XRD patterns of GC#4 heat-treated at condition B and C

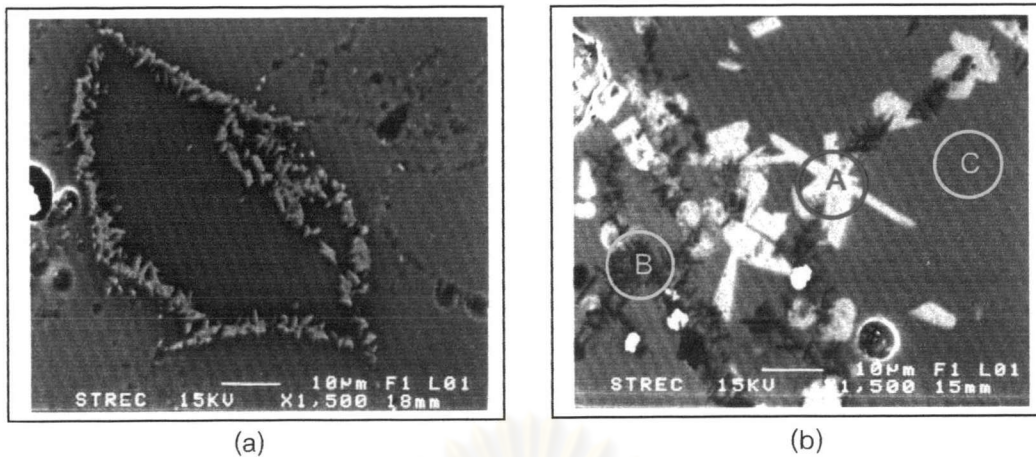


Fig.4.34 SEM micrographs (1500x) of wollastonite-ferroan and anorthite phase observed in GC#4 after heat-treatment at condition B (a) C (b)

After heat-treatment at condition B, no crystalline peak was detected as shown in the XRD pattern. However, very small acicular crystals were observed in the SEM micrograph indicating that the crystals actually formed after heat-treatment at condition B. The crystalline peaks of wollastonite-ferroan and anorthite phases were identified by XRD pattern after heat-treatment at condition C. Two distinct crystal morphologies of acicular crystals and dark dendritic crystals were observed in SEM micrograph after heat-treatment at condition C. The compositions of the acicular crystal, the dark dendritic crystal and the glassy matrix were examined by EDS. The EDS spectrums, spotted on the acicular crystal area (A), dark dendritic crystal area (B) and glassy matrix area (C), of GC#4 heat-treated at condition C, are shown in Fig.D-26, Fig.D-27 and Fig.D-28 in Appendix D, respectively. The EDS analysis showed that the acicular crystals contain mainly Si, Ca and Fe confirming wollastonite-ferroan ($\text{Ca}_{2.87}\text{FeO}_{0.13}(\text{SiO}_3)_3$), the dark dendritic crystals contain mainly Si, Al and Ca confirming anorthite ($\text{Ca}(\text{Al}_2\text{SiO}_8)$), as identified by XRD technique whereas the glassy matrix enriched in Si, Al, Na with poor in Ca. The XRD patterns of GC#11, GC#9 and GC#12 heat-treated at condition B and C are shown in Fig.D-29, Fig.D-30 and Fig.D-31, respectively.

2. Mixed phased of cristobalite, quartz and wollastonite-ferroan

The mixed phases of cristobalite, quartz, and wollastonite-ferroan were found in GC#7, GC#8, GC#15, GC#19 GC#16 and GC#20. The compositions of these glass-ceramics enriched of SiO_2 with medium amount of CaO as shown in Table 4.8.

Table 4.8 Compositions of glass-ceramics contained cristobalite, quartz and wollastonite-ferroan

GC#	SiO_2	B_2O_3	Na_2O	CaO	MgO	ZnO	Al_2O_3	Fe_2O_3
7	63	5	15	10	0	3	1	3
8	59	5	15	10	0	3	5	3
15	64	5	5	15	0	1	5	5
19	64	5	10	10	0	3	5	3
16	58	15	10	10	0	1	1	5
20	56	15	10	10	0	3	1	5

The XRD patterns of GC#19 heat-treated at condition B and C are shown in Fig.4.35. The microstructures of GC#19 heat-treated at condition B and C are shown in Fig.4.36 (a) and (b), respectively.

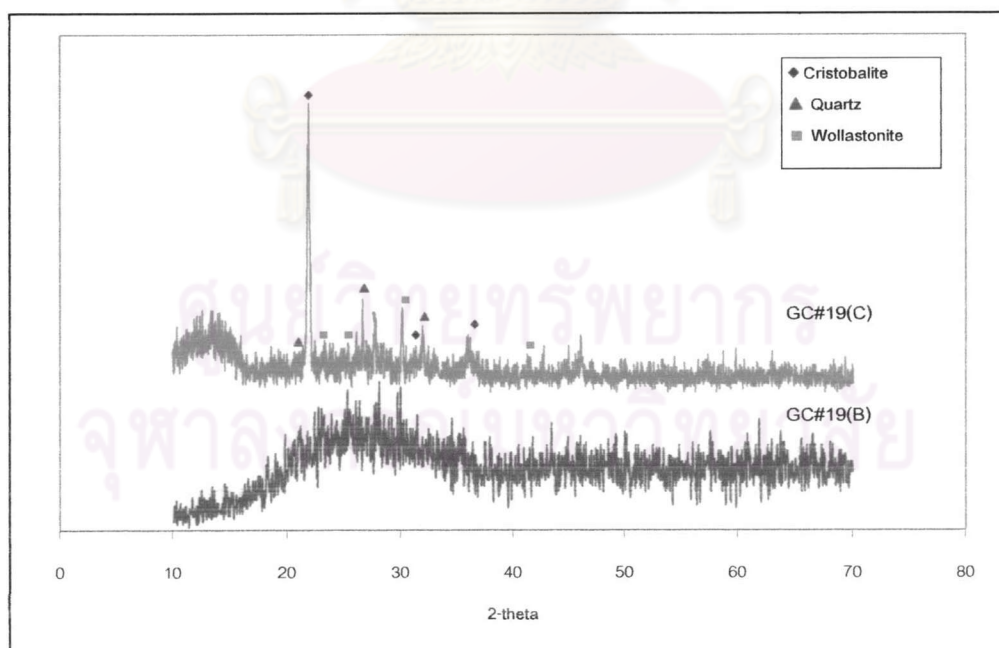


Fig.4.35 XRD patterns of GC#19 heat-treated at condition B and C

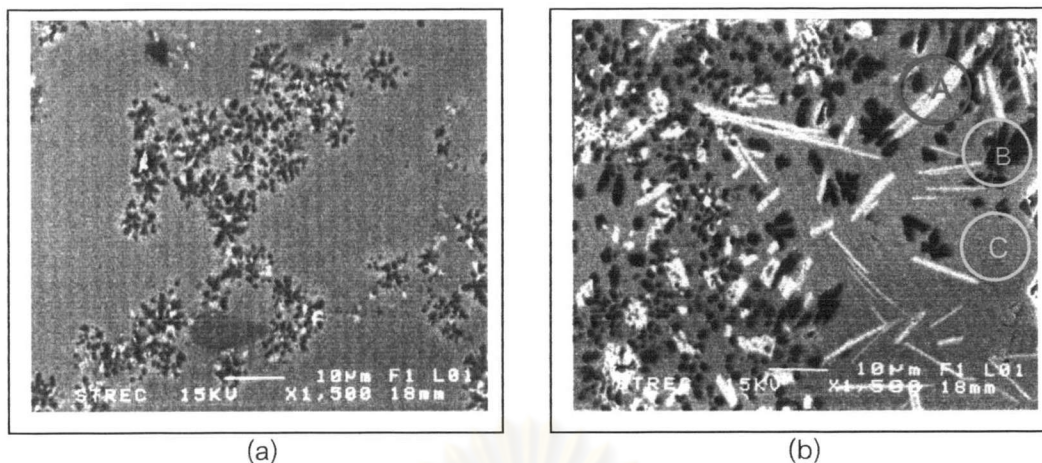


Fig.4.36 SEM micrographs (1500x) of cristobalite, quartz and wollastonite-ferroan phase observed in GC#19 after heat-treatment at condition B (a) C (b)

After heat-treatment at condition B, no detected crystalline peak was observed in the XRD pattern. However, very small flower-like crystals were observed in the SEM micrograph indicating that the crystals actually formed after heat-treatment at condition B. The crystalline peaks of cristobalite, quartz and wollastonite-ferroan phases were identified after heat-treatment at condition C as shown in the XRD pattern. Two distinct crystal morphologies of acicular crystals and dark flower-like crystals were observed in SEM micrograph after heat-treatment at condition C. The compositions of the acicular crystal, the dendritic crystal and the glassy matrix were examined by EDS. The EDS spectrums, spotted on the acicular crystal area (A), dark flower-like crystal area (B) and glassy matrix area (C), of GC#19 heat-treated at condition C, are shown in Fig.D-32, Fig.D-33 and Fig.D-34 in Appendix D respectively. The EDS analysis showed that the acicular crystals contain mainly Si, Ca and Fe confirming wollastonite-ferroan ($\text{Ca}_{2.87}\text{FeO}_{0.13}(\text{SiO}_3)_3$) as identified by XRD technique whereas the glassy matrix enriched in Si, Al, Na with poor in Ca. The EDS spectrums spotted on the flower-like crystal show very large content of Si. It is difficult to distinguish quartz and cristobalite by EDS. It is believed that the flower-like crystals could be either the crystal of quartz or cristobalite.

The XRD patterns of GC#7 and GC#15 heat-treated at condition B and C are shown in Fig.D-35 and Fig.D-36. The XRD patterns and the SEM micrograph of GC#8 heat-treated at condition B and C are shown in Fig.D-37 and Fig.D-38 (a) and (b), respectively. The mixed phases of cristobalite and quartz with large portion of amorphous phase were found in GC#16 and GC#20. The XRD patterns of these glass-ceramics heat-treated at condition B and C are shown in Fig.D-39 and Fig.D-40, respectively.

It is noticeable from all twenty-five glass-ceramics that the size of crystals developed with the increasing of heat-treatment temperature. The crystalline peaks of crystal phases in the XRD patterns were clearly seen (high intensity, sharp and narrow) after heat-treatment at condition C.

4.3.3. Mechanical property

The bending strength obtained from twenty-five glass-ceramics after heat-treatment at condition B and C are shown in Fig.4.37.

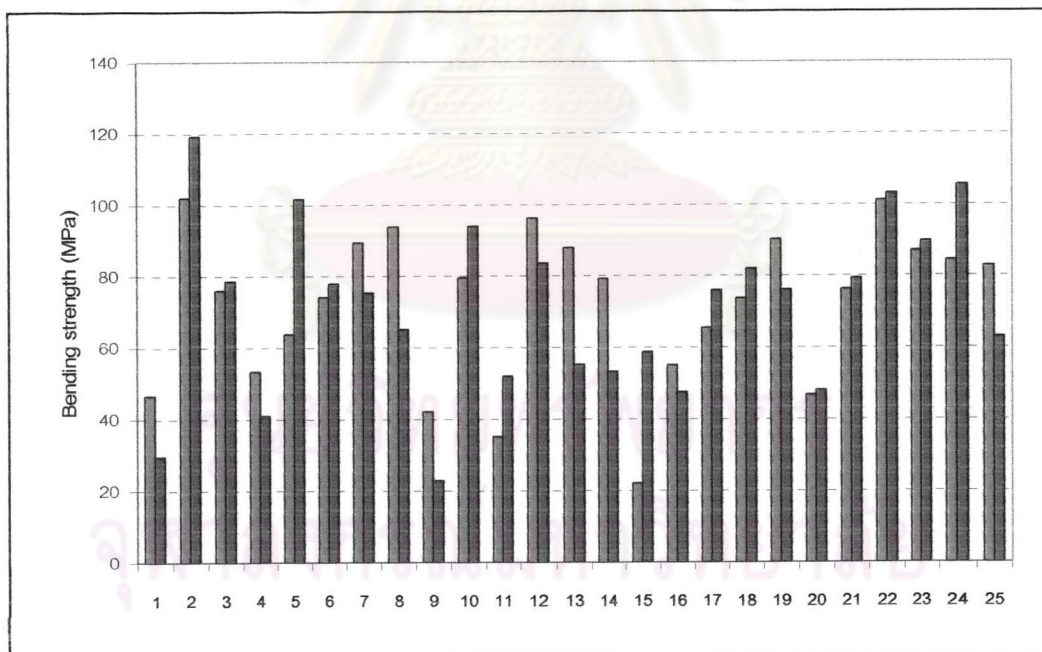


Fig.4.37 Three point bending strength of twenty-five glass-ceramics after heat-treatment at condition B(■) and C (■)

It was found that not all of glass-ceramics heat-treated at condition C gives the bending strength higher than condition B. The bending strength of eleven glass-ceramics heat-treated at condition C was lower than condition B. Thus the bending strength does not greatly depend on heat-treatment temperature.

There are many factors possibly influence the strength of glass-ceramic, such as porosity, flaw, crystal morphology and the mismatch of thermal expansion coefficient between the crystals and glassy matrix. The presence of pores strongly influence on the strength of glass-ceramics not only because they reduce the cross-section area over which the load is applied, but more importantly they act as stress concentrators [27]. As the load is applied on the samples, open pores on the surface can be the origin of crack propagation. Flaws generally occur on a free surface and have a wide distribution of lengths. The strength of glass is not intrinsic to its composition, but may depend greatly on method of processing [10]. Thus it is difficult to discuss specifically on what factor actually affects the strength of each glass-ceramic. As we have known that the strength of glass-ceramics usually higher than those of glasses, since the crystals present in the glass-ceramics tend to limit the size of the flaws present in the material, increasing its strength. The presence of the crystalline also enhances toughness [27, 29]. However, since glass-ceramics are composed of two difference phases, glassy phase and crystal phase, the mismatch of thermal expansion coefficient developed during the cooling process resulting in the large residual stresses.

It is noted that our glass-ceramic samples have been polished to smooth the surface before subjected to the three point bending test. Therefore, as the surface of samples was eliminated, closed pores became opened pores on the polished surface. In addition, during the polishing process, surface flaws can be accidentally introduced onto the samples. In this study, glass-ceramics contained single crystalline phase of wollastonite and pyroxene show higher strength than glass-ceramics contained mixed phases. The bending strength and crystal phase formation of glass-ceramics heat-treated at condition B and C are shown in Table 4.9. The results were classified by type of crystalline.

Table 4.9 The bending strength of glass-ceramics heat-treated at condition B and C

GC#	Condition B		Condition C	
	Crystals	Strength (Mpa)	Crystals	Strength (Mpa)
1	W/Am	46.6 ± 5.8	W	29.7 ± 4.9
10	W/Am	79.6 ± 20.1	W	94.0 ± 4.2
24	W	84.4 ± 6.6	W	105.5 ± 17.2
23	W	87.0 ± 1.7	W	89.7 ± 7.3
5	P	63.8 ± 11.8	P	101.6 ± 19.8
17	P/Am	65.4 ± 12.1	P	76.0 ± 7.6
18	P	73.8 ± 12.0	P	82.0 ± 6.5
6	P	74.2 ± 11.5	P	78.0 ± 8.3
3	P	76.0 ± 9.0	P	78.7 ± 9.2
21	P	76.2 ± 11.9	P	79.3 ± 14.5
25	P/Am	82.8 ± 7.5	P	63.0 ± 10.3
22	P	101.1 ± 14.4	P	103.1 ± 18.2
2	P	102.0 ± 15.6	P	119.3 ± 21.0
14	Am	79.2 ± 8.4	C	53.4 ± 6.7
13	Am	88.0 ± 14.9	C	55.3 ± 7.3
11	A/Am	35.2 ± 6.6	W/A	52.0 ± 8.1
9	A	42.2 ± 4.8	A/Am	23.0 ± 9.1
4	A/Am	53.5 ± 10.8	W/A	41.1 ± 15.5
12	A/Am	96.3 ± 20.0	A	83.6 ± 4.5
20	Am	46.8 ± 5.4	C/Q	48.2 ± 14.3
16	Am	55.2 ± 11.3	C/Q	47.7 ± 11.4
7	C	89.5 ± 16.2	C/Q/W	75.4 ± 16.6
8	C	93.92 ± 16.48	C/Q/W	65.17 ± 10.6
15	Am	22.0 ± 1.8	C/Q/W	58.8 ± 11.9
19	Q/Am	90.23 ± 14.8	C/Q/W	76.17 ± 25.8

The highest bending strength obtained from this study is the bending strength of GC#2 heat-treated at condition C (contained pyroxene phase), which is ~119.26 MPa. The bending strength of GC#2 is also the highest after heat-treatment at condition B, which is ~101.96 MPa. It is noticeable that the bending strength of GC#22, GC#5 (contained pyroxene phase) and GC#24 (contained wollastonite phase) are comparable to the bending strength of GC#2. The bending strength of GC#22 heat-treated at condition B and C is ~101.10 and 103.11 MPa, respectively. The bending strength of GC#24 and GC#5 heat-treated at condition C is ~105.52 and 101.64 MPa, respectively.

The bending strength of glass-ceramics contained mixed phases is noticeable lower than glass-ceramics contained single phase. The lowest bending strength obtained from this study is the bending strength of GC#9 heat-treated at condition C, which is ~22.96 MPa. The bending strength of GC#1 heat-treated at condition C is considerably low as well as GC#9, which is ~29.67 MPa. According to the physical properties, it was observed that GC#1 and GC#9 over fired after heat-treatment at condition C. The over fired characteristic can degrade the strength of glass-ceramics because of the increasing of close pores and bubbles.

It is noticeable that the bending strength of glass-ceramics contained single phase obtained after heat-treatment at condition C is higher than condition B, whereas the bending strength after heat-treatment at condition C of glass-ceramics contained mixed phase is lower than condition B. The bending strength of single phase glass-ceramics (wollastonite and pyroxene) heat-treated at condition B and C are shown in Fig.4.38. The bending strength of mixed phases glass-ceramics heat-treated at condition B and C are shown in Fig.4.39. Note that the bending strength of glass-ceramics shown in these figures excluding the over-fired glass-ceramics.

จุฬาลงกรณ์มหาวิทยาลัย

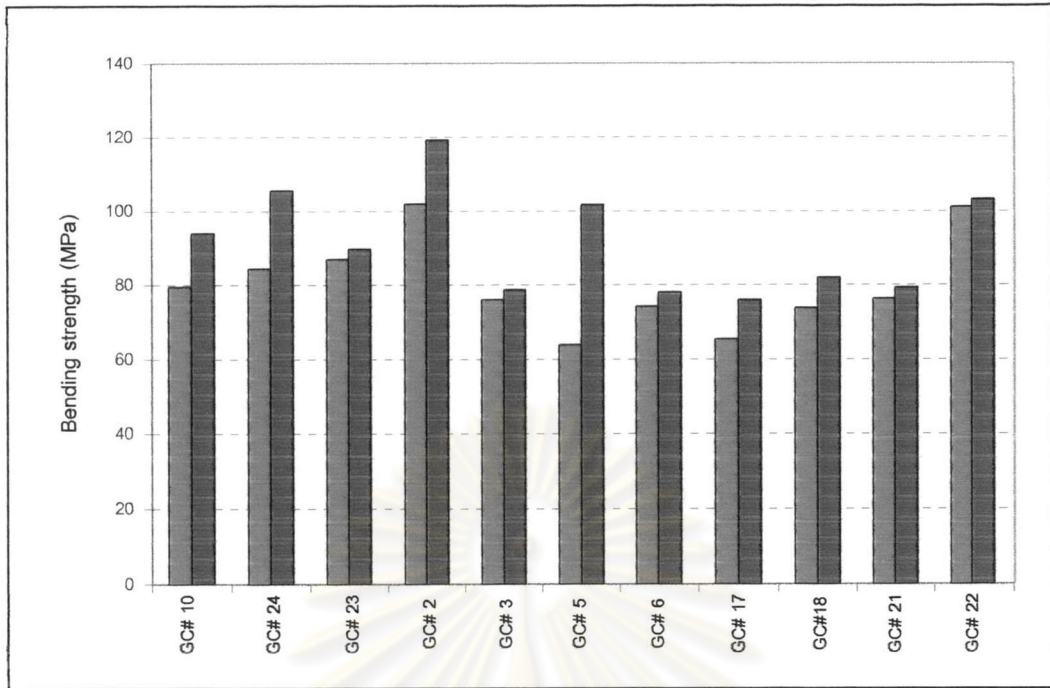


Fig.4.38 The bending strength of single phase glass-ceramics heat-treated at condition B (■) and C (■)

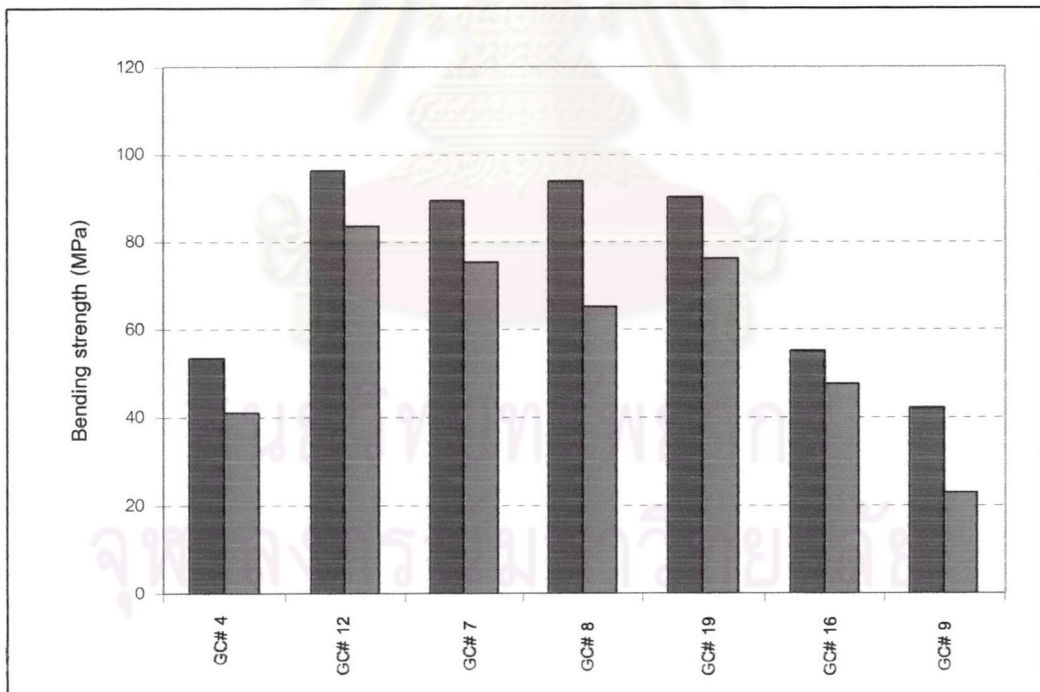


Fig.4.39 The bending strength of multiple phase glass-ceramics heat-treated at condition B (■) and C (■)

According to XRD and SEM results, the size of crystals increased with the increasing of the heat-treatment temperatures in either single or mixed phases glass-ceramics. Thus it can be explained in two different ways, the bending strength of single phase glass-ceramics increased with the increasing of crystals size whereas the bending strength of mixed phases decreased.

In general, the formation of crystals in glasses enhances the strength under the condition of uniform distribution in glassy matrix and uniform crystal size. Therefore, it is believed that the bending strength degradation of mixed phases might come from the non-uniform of both distribution and crystal size, since they contained different crystal phases. In addition, the bending strength decrease can be due to the shear stresses arising from the difference in the thermal expansion coefficient between the crystals and the residual glass phase. Thus the differences of phases formed in the samples cause large mismatch of thermal expansion coefficient and generate large residual stresses. When the boundary shear stresses development become greater than the strengthening resulting from the crystals, the development of the crystal size can be ignored, then the strength decreases.

4.3.4. Chemical durability

According to zinc waste contained significant amount of heavy metal that is lead (Pb), therefore it was very important to examine the leachability characteristic of Pb in glass-ceramics matrix. It is noted that the regular standard of heavy metal leached out concentration is different in difference countries. The Italian limit of the leached out concentration of Pb is 0.2 ppm, the Korean limit is 1 ppm and the Taiwanese limit is 5 ppm [4, 21, 28]. In Thailand, there is no regular standard of heavy metal leached out concentration, thus the USA regulatory limit was selected to use as a standard in this study. The American EPA's toxic characteristic leaching procedure (TCLP) method 1311 was used to examine the chemical stability of glass-ceramics in terms of leaching of heavy metals ions. The concentration of Pb in the leachate of glass-ceramics was compared with the USA regulatory limits (5 ppm) [4].

Chemical durability is usually referred to the resistance of the glass surface to chemical agents. In general, the durability reaction begins at the surface and spreads inwards as a result of either the diffusion of the invading elements into the glass or the breakup of the glass network bonds by the attacking species. Hence, the mechanism of attack includes leaching of mobile ions out of glass, uniform dissolution of the glass network and preferential dissolution of glass. During leaching, invading ions from the fluid medium enter the glass structure through the interstices and exchange sites with host ions in the glass. Then the host ions gradually move to the glass surface. These mechanisms call "leaching". Alkali ions are the most mobile ions in the glass, leaching of alkali ions is the dominant durability problem [10].

Glass-ceramics are composed of two distinct phases, which are crystal and residual glass phase. Thus the chemical durability of glass-ceramic is the chemical durability of the crystal and the residual glass phase. The compositions of crystal usually differ from the residual glass, which causes the preferential dissolution during leaching test. Preferential dissolution is the leachability of different phases. If some phases of glass contain compositions that are more readily attacked by the medium than others, the ratio of the dissolved species in the medium would be different from that of parent glass.

Therefore the effect of crystal phase formation on the leachability of Pb was discussed. The leached out concentration of Pb from glass-ceramic matrix heat-treated at condition B (650°C for 1 hour and 750°C for 2 hours) and C (750°C for 1 hour and 850°C for 2 hours) are shown in Table 4.10. Note that the TCLP test was conducted on the pulverized specimens. The results were classified by type of crystalline.

Table 4.10 Leached out concentration of Pb in glass-ceramics

GC#	Condition B		Condition C	
	Crystalline	Concentration (ppm)	Crystalline	Concentration (ppm)
1	W/Am	3	W	2
10	W/Am	11	W	7
24	W	2	W	2
23	W	2	W	2
5	P	2	P	22
17	P/Am	17	P	17
18	P	21	P	32
6	P	20	P	42
3	P	14	P	26
21	P	21	P	23
25	P/Am	34	P	50
22	P	27	P	20
2	P	18	P	18
14	Am	2	C	4
13	Am	2	C	4
11	A/Am	11	W/A	2
9	A	13	A/Am	11
4	A/Am	9	W/A	2
12	A/Am	2	A	8
20	Am	18	C/Q	20
16	Am	2	C/Q	2
15	Am	21	C/Q/W	17
7	C	19	C/Q/W	2
19	Q/Am	14	C/Q/W	2
8	C	18	C/Q/W	6

It is very interesting that the leached out concentrations of Pb in glass-ceramics contained pyroxene phase heat-treated at condition B and C were very high and none of them gave the leached out concentration of Pb lower than 5 ppm, which is the limit required by the EPA of USA. However, many of glass-ceramics obtained in this study gave the leached out concentration of Pb lower than the limit. The leached out concentrations of Pb in six glass-ceramics, which are GC#1, GC#24, GC#23, GC#16, GC#14 and GC#13, are lower than the limit in both heat-treated at condition B and C. The highest of Pb concentration were found in GC#25, which is 34 ppm and 50 ppm after heat-treatment at condition B and C, respectively.

The effect of heat-treatment temperature on leachability of Pb was considered. Pb concentration of glass-ceramics contained single wollastonite phase trended to decreasing as the temperature increases (condition B > C). Pb concentration of glass-ceramics contained single pyroxene and cristobalite phase trended to increasing as the temperature increases (condition B < C). Pb concentration of glass-ceramics contained multiple phase at condition C was mostly lower than condition B.

4.3.5. Coefficient of thermal expansion

In this study, it is noted that difference temperature ranges were used to determine the thermal expansion coefficient by considering the only the range of graph between $dL/dL_0\%$ and temperature that show straight slope. Thermal expansion of twenty-five glass-ceramics heat-treated at condition C (750°C for 1 hour and 850°C for 2 hour) is shown in Table 4.11. The results were classified by type of crystalline.

ศูนย์วิทยทรัพยากร
จุฬาลงกรณ์มหาวิทยาลัย

Table 4.11 Thermal expansion coefficient of glass-ceramics

GC#	Crystal	Temperature (°C)	α COE ($\times 10^{-6}/^{\circ}\text{C}$)
1	W	100-350	12.2
10	W	100-350	12.2
24	W	100-350	13.7
23	W	100-350	14.3
5	P	100-350	13.7
17	P	100-350	13.8
18	P	100-350	13.9
6	P	100-350	14.4
3	P	100-350	14.3
21	P	100-350	13.4
25	P	100-350	13
22	P	100-350	12.4
2	P	100-350	15.5
14	C	200-400	11.2
13	C	200-400	12.0
11	W/A	100-350	11.8
9	A/Am	100-350	12.5
4	W/A	100-350	13.5
12	A	100-350	12.4
8	C/Q/W	100-350	12.5
15	C/Q/W	100-350	12.2
20	C/Q	100-200	11.7
16	C/Q	200-400	10.7
19	CW/Q	200-400	13.5
7	C/Q/W	200-400	8.4
19	CW/Q	200-400	13.5

The general, the addition of alkaline oxide into silicate glass increases the thermal expansion coefficient. This is because the addition of alkaline oxide increases the number of non bridging oxygen causing the un-symmetry of Si-O bond, the substitution of interstices sites and the prevention of bond bending. When Na₂O was replaced by CaO with a fixed amount of SiO₂, the strength of glass-structure is increased causing the decreasing in thermal expansion coefficient. Consider the addition of MgO compared with the addition of Na₂O and. Since the field strength of MgO is higher than those of CaO and Na₂O, the capability of reducing thermal expansion of MgO is lower than those of CaO and Na₂O. Thus the capability of reducing thermal expansion of oxides can be ordered as Mg<Ca<Sr<Ba [27].

Unlike the simple glass composition, the compositions of the initial glass in this study were varied in eight different oxides that considerably complex oxide compositions. Therefore, it is difficult to explain the variation of thermal expansion coefficient as the function of oxide compositions.

In this study, we have found that thermal expansion coefficient is difference by the type of crystal. GC#2 contained pyroxene phase gave the highest thermal expansion coefficient, which is $\sim 15.5 \times 10^{-6}/^{\circ}\text{C}$ in the temperature range of 100-350^oC whereas GC#7 contained mixed phases of quartz, cristobalite and wollastonite gave the lowest thermal expansion coefficient, which is $\sim 8.4 \times 10^{-6}/^{\circ}\text{C}$ in the temperature range of 200-400^oC. Thermal expansion coefficient of single phase glass-ceramics was in the vicinity whereas of multiple glass-ceramics was varied.

ศูนย์วิทยทรัพยากร
จุฬาลงกรณ์มหาวิทยาลัย